SubZero: A Sea Ice Model with an Explicit Representation of the Floe Life Cycle

Georgy E. Manucharyan and Brandon P. Montemuro

School of Oceanography, University of Washington, Seattle, WA

Key Points:

- This paper is a non-peer reviewed preprint submitted to EarthArXiv and has been submitted for publication to the Journal of Advances in Modeling Earth Systems (JAMES) for peer review. Subsequent versions of this manuscript may have slightly different content.

Corresponding author: Georgy Manucharyan, `gmanuch@uw.edu`

Abstract

Sea ice dynamics exhibit granular behavior as individual floes and fracture networks become particularly evident at length scales O(10–100) km and smaller. However, climate models do not resolve floes and represent sea ice as a continuum, while existing floe-scale sea ice models tend to oversimplify floes using discrete elements of predefined simple shapes. The idealized nature of climate and discrete element sea ice models presents a challenge of comparing the model output with floe-scale sea ice observations. Here we present SubZero, a conceptually new sea ice model geared to explicitly simulate the life cycles of individual floes by using complex discrete elements with time-evolving shapes. This unique model uses parameterizations of floe-scale processes, such as collisions, fractures, ridging, and welding, to simulate a wide range of evolving floe shapes and sizes. We demonstrate the novel capabilities of the SubZero model in idealized experiments, including uniaxial compression, the summer-time sea ice flow through the Nares Strait, and winter-time sea ice growth. The model naturally reproduces the statistical behavior of the observed sea ice, such as the power-law appearance of the floe size distribution and the long-tailed ice thickness distribution. The SubZero model could provide a valuable alternative to existing discrete element and continuous sea ice models for simulations of floe interactions.

Plain Language Summary

Sea ice is an inherent part of our climate system that responds rapidly to climate change. It is commonly conceptualized as a collection of many strongly interacting floes (sea ice fragments). However, climate models treat sea ice as a continuum, as resolving the complexity of floe-scale mechanical and thermodynamical processes is challenging. Here we present a conceptually new sea ice model that can explicitly simulate the life cycle of individual sea ice floes, including collisions, fractures, ridging and rafting, welding, and growth. We demonstrate the novel capabilities of SubZero in idealized experiments, including simulations of summer-time sea ice flow through a narrow strait and winter-time sea ice growth. Both experiments were successful in reproducing the statistical behavior of the observed sea ice, specifically the distribution of floe sizes and thicknesses. The unique SubZero capabilities may improve the realism of sea ice modeling.

1 Introduction

Sea ice motion at relatively large scales, O(100 km), is commonly represented in climate models (Keen et al., 2021) using continuous rheological models (Hibler, 1979; Coon, 1980). However, at relatively small scales, O(10–100) km and smaller, sea ice can be viewed as a granular material consisting of a collection of interacting floes (Rothrock & Thorndike, 1984; Toyota et al., 2006; Perovich & Jones, 2014; Zhang et al., 2015; Roach et al., 2018; Stern et al., 2018). The discrete floe dynamics are particularly pertinent in marginal ice zones where interacting floes are distinctly observed in satellite images, and sea ice resembles granular material (Figure 1). In consolidated pack ice, floes can be frozen to each other (welded) but externally forced large-scale sea ice motion can occur due to frequent anisotropic fractures and deformation (Hibler III & Schulson, 2000; Hutchings et al., 2011). Since specific floe configurations, their mechanical properties, and existing fracture networks are expected to affect the short-term evolution of sea ice, explicitly representing these features in some models is desirable.

Although it is technically possible to run continuum sea ice models at very high resolutions that approach floe scales, the model equations are formally applicable under the assumption that the grid box size is significantly larger than the characteristic floe size. Under this assumption, the floe interactions can be represented statistically (Hibler III, 1977; Feltham, 2008). Nonetheless, high-resolution numerical simulations can generate discontinuities that resemble observed linear kinematic features (Hutter & Losch, 2020;

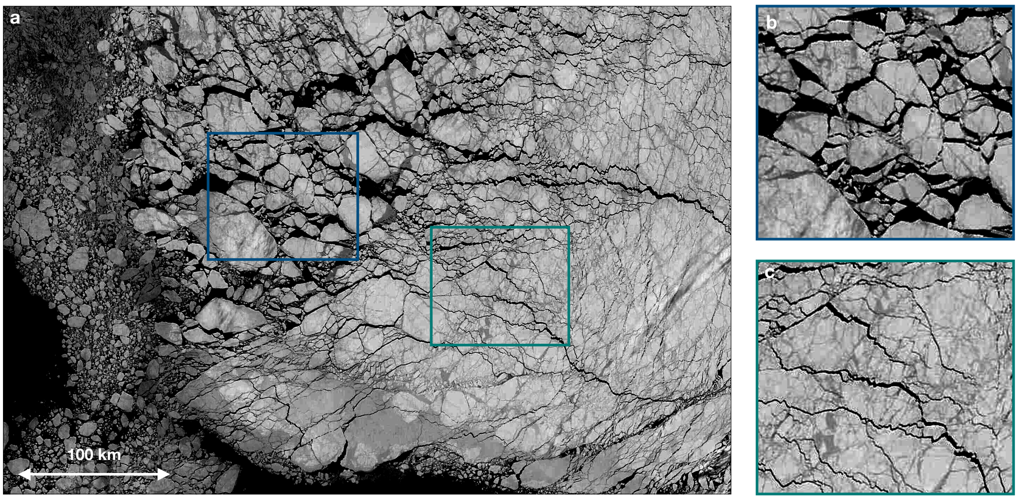

Figure 1. Example of the summertime sea ice in the Beaufort Sea, near Banks Island demonstrating its granular discontinuous nature and spatial heterogeneity. **(a)** A filtered reflectance image from the NASA WorldView website encompassing a region about 550 by 350 km in size bounded by 71–76^{o}N in latitude and 126-137^{o}W in longitude, taken on May 17th, 2021. The image filtering included making it gray scale and adjusting the level curves to highlight the fracture network and individual floes. **(b,c)** Zoomed-in view of the rectangular regions about 100 by 100 km in size as denoted in **(a)**.

Mohammadi-Aragh et al., 2020; Mehlmann et al., 2021; Hutter et al., 2022). But despite the major progress of continuous modeling of large-scale sea ice and the ongoing developments in pushing their applicability limits by increasing the resolution, the rheological models are not meant to represent the scales of motion at which individual floes start to affect dynamics (Coon et al., 2007). Essentially, continuous models are not designed to generate the highly fragmented sea ice as shown in Figure 1. Hence, the validation against floe-scale observations for continuous models is only possible using statistical characteristics or large-scale sea ice motion because the rheological parameters parameterize the cumulative effects of floe interactions. Consequently, direct comparisons of continuous models to remote sensing or field observations of individual floe behavior are challenging, even considering that sea ice motion is inherently stochastic (Lemke et al., 1980; Percival et al., 2008; Rampal et al., 2009).

Alternatives to continuous rheology models are Discrete Element Models (DEMs), developed initially in the context of granular assembles and rock dynamics (Cundall & Strack, 1979; Potyondy & Cundall, 2004). DEMs represent media as a collection of a large number of colliding bonded elements of specified shapes and contact laws and hence are typically computationally demanding. Since the continuous equations of motion are often unknown, DEMs resort to specifying the interaction laws between its elements and strive to calibrate them using macro-scale observations or laboratory experiments (Grima & Wypych, 2011). Another way of simulating fluid motion with known rheology is the Smoothed Particle Hydrodynamics approach that also simulates particle motion but the laws of their interaction are derived from the continuous fluid rheology (Monaghan, 1992; Gutfraind & Savage, 1997; Lindsay & Stern, 2004; Marquis et al., 2022). As such, DEMs present a more general class of models that could simulate media for which corresponding macro-scale rheology might not exist, provided that the interaction laws between its particles could be constrained from observations.

With increasing computational capabilities and the emergence of comprehensive field and remote sensing observations at the floe-scale, the DEM approach (Cundall & Strack, 1979) has been adapted for modeling discontinuous sea ice dynamics (Hopkins et al., 2004; Wilchinsky et al., 2010; Herman, 2013, 2016; Kulchitsky et al., 2017; Damsgaard et al., 2018; Liu & Ji, 2018; Tuhkuri & Polojärvi, 2018; West et al., 2021). At engineering scales, below about O(10-100) m, sea ice DEMs have implemented a bonded particle model (Liu & Ji, 2018; Tuhkuri & Polojärvi, 2018). At these scales, the models could be cross-validated with laboratory experiments, specialized field observations, and measurements of stress from structure-ice interactions, including ships. Sea ice DEMs have also been used for exploring idealized processes, including jamming and ice bridge formation in straits (Damsgaard et al., 2018) and wave-floe interactions (Herman et al., 2019). At larger regional scales, up to a few 100 km, the CRREL model (Hopkins et al., 2004; Wilchinsky et al., 2010) and its recent modification that utilizes level sets to compute collisions (Kawamoto et al., 2016) has been adapted for regional simulations of Nares Strait (West et al., 2021). The Siku model (Kulchitsky et al., 2017) is capable of simulating the formation of basin-scale linear kinematic features in the Beaufort Gyre associated with the coastal features. DEMs are computationally demanding due to requiring a large number of particles and small computational time steps. As such, their use in coupled Earth system models is challenging but can be done. One example of a prototype large-scale sea ice model within (global) Earth system models currently under development is DEMSI (Turner et al., 2022).

Existing sea ice DEMs [see Tuhkuri and Polojärvi (2018) for a review] follow a conventional approach of using simple pre-defined shapes for the elements, e.g., points or disks (Herman, 2013; Damsgaard et al., 2018; Chen et al., 2021), polygons (Kulchitsky et al., 2017) or tetrahedra (Liu & Ji, 2018). However, observations demonstrate that floes range dramatically in shapes and sizes (Figure 1) and evolve in time subject to a variety of processes like fractures, rafting and ridging, lateral growth/melt, welding, etc. Hence, using pre-defined element shapes brings some ambiguity about what elements and bonds between them physically represent. Are elements supposed to approximate the behavior of aggregates of floes (similar to what continuous rheological models are assuming), or perhaps they are representing bonded constituents of floes or some other metric of a sea ice state? Without a robust understanding of what a DEM element represents, it is difficult to search for direct correspondence between the state variables of the DEM and the observed sea ice. These are challenging questions, and the answers depend on the modeling philosophy because sea ice is a multi-scale media where grains are not well defined.

This manuscript presents a prototype for a conceptually new discrete element approach to sea ice modeling that relies fundamentally on using elements with evolving boundaries to more realistically represent the floe life cycle by modeling the creation, growth/melt, welding, and break-up of individual pieces of sea ice. Our goal is to develop a model that could be used in conjunction with floe-scale satellite and in situ observations for floe-scale sea ice predictions and process studies. While the ice floe model consists of several mechanical and thermodynamic components, our ultimate focus is on developing a set of floe interaction rules that could lead to realistic sea ice mechanics, including distributions of floe sizes, thicknesses, and shapes. In contrast with existing sea ice DEMs that use prescribed simple shapes of elements (like disks), our approach is based on more realistic floes conceptualized as complex-in-shape time-evolving elements instead of specifying a large number of stiffly-bonded simple elements to represent floes. We argue that the model capability of developing floe shapes naturally, due to specific physical processes at play, might bring us closer to direct model validation with floe-scale observations. The numerical implementation of our proposed method is publicly available as the SubZero sea ice model on GitHub (Manucharyan & Montemuro, 2022), and its releases are published on Zenodo (Montemuro & Manucharyan, 2022). Below, we provide the model formulation and present a few idealized simulations to showcase the novel capabilities.

Table 1. A list of prognostic and diagnostic variables that define the state of a floe in the SubZero model.

Floe variable	Description
area	Floe area
h	Floe thickness
mass	Floe mass
c_alpha	Rotated floe vertices relative to geometric center of area
c_0	Unrotated floe vertices relative to geometric center of area
inertia_moment	Floe moment of inertia
angles	Interior angles of floe corresponding to vertices of c_0/c_alpha
rmax	Maximum distance from geometric center of area to a floe vertex
StressH	History of instantaneous stress tensors on a floe
Stress	Average of instantaneous stress tensors on a floe
FxOA, FyOA	X & Y component of forces per unit area from Ocean and Atmosphere
torqueOA	Torque per unit area from Ocean and Atmosphere
X, Y	X & Y location of Monte-Carlo points in unrotated plane
A	Logical matrix saying if location [X,Y] is inside floe shape
alive	Logical value describing if floe is alive or will be discarded
X_i, Y_i	X & Y location of floe geometric center of area
alpha_i	Rotation value of floe from original unrotated position
Ui, Vi	Velocity of centroid of floe in X & Y direction
ksi_ice	Angular velocity of floe
d{Xi,Yi,...}_p	Time rate of change of X_i, Y_i,... previous time step
interactions	List of interactions with other floes
potentialInteractions	List of all potential interactions with other floes
collision_force	Summation of all forces from interactions with other floes
collision_torque	Summation of all torques from interactions with other floes
OverlapArea	Summation of all overlapping area with other floes

2 SubZero model philosophy

In contrast with existing sea ice DEM methods, our sea ice DEM simulates the motion of elements that change their shapes, much like the observed sea ice floes do during interactions with other floes or boundaries. SubZero keeps a data structure tracking a set of necessary state variables for each individual floe. The complete list of state variables is included in Table 1. Crucially, the ability of model elements to change shape is not simply an additional improvement over existing DEMs that use fixed element shapes but something that leads to fundamentally different dynamics of floe interactions. Specifically, closely-packed concave elements in our model can lead to interlocking behavior: floes appearing like rigid puzzle pieces cannot substantially move relative to each other except when they are allowed to fracture. For such interlocked floes, the relative motion can only occur if floes undergo area-reducing processes such as deformations induced by micro- and macro-scale fractures (for example, ridging/rafting). Consequently, bonds between the interlocked elements are not entirely necessary as their role is partially transferred towards parameterizations of floe fractures and other processes that change the shape of individual floes. We hypothesize that a DEM formulation based on floe shape evolution would make the model comparisons with observed floes less ambiguous.

The increased complexity of floe interaction physics is the trade-off for using elements with freely evolving shapes. Floes undergo many processes that affect their shapes, including fracturing, ridging/rafting, and welding, making them concave. In addition, the fracture process, which is essential to the model dynamics, rapidly increases the num-

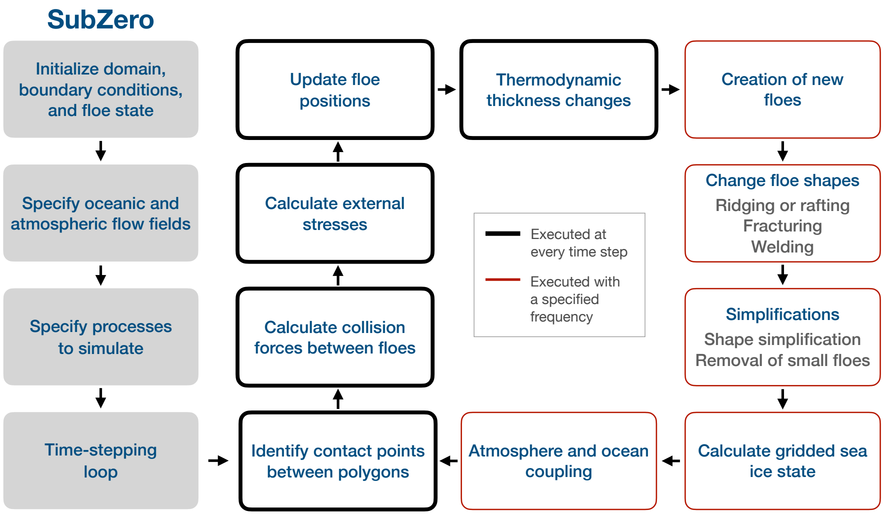

Figure 2. Operational flow chart for the SubZero sea ice model. The shaded gray boxes represent the different sections of the program, the red outlined boxes are processes that are executed every at specified intervals, and the black outlined boxes are processes that occur at every time-step.

ber of floes. To avoid an explosion of the number of floes in a model, it is necessary to model only sufficiently large floes and treat sufficiently small floes as unresolved. This means that we remove any floe with an area below a designated minimum floe size from the model and put this mass into a separate array to track. Conventional DEMs can also generalize floes as a set of fixed-shaped elements that are bonded together, but the difference with our SubZero model is that by representing the complex floe shapes by their polygonal boundaries, bonds are not needed to simulate the interactions of elements covering its surface area. In other words, the trade-off in representing floes is between using a large number of simple fixed-shape elements with simple interaction rules versus representing it with a single complex-shaped polygon and complex physics describing its shape changes upon interactions with other floes. While using concave shape-changing floes as elements in a sea-ice DEM may lead to improved realism of simulations, it also creates new challenges in numerical integration and parameterizations of floe-scale physics that we address below.

3 Dynamical core of the SubZero model

Below we describe the essential components of the model, providing a relatively basic representation of crucial sea ice processes acting at the floe scale (see Figure 2 for the simulation workflow). Our modeling philosophy envisions iterative improvements of its components upon input from a broad sea ice research community as the model is used in conjunction with observational, experimental, modeling, and theoretical studies.

3.1 Floes as polygons with changing boundaries

Motivated by observations of sea ice fracture networks and floe boundaries that appear piece-wise linear (Figure 1), we choose to use the polygonal representation of floes. The model homogenizes sea ice properties, such as the thickness within the floe, such that its polygonal shape defines the center of mass, total volume, and moment of inertia. The floes (i.e., their vertex coordinates) are translated following the velocity and angular velocity of the floe, which are calculated using the momentum and angular momentum equations written for individual floes (Section 3.3). The model has the capability of splitting floes into rigidly connected sub-floes to keep track of floes that were ridged and/or welded together, with each sub-floe carrying its own properties, like thickness. However, this configuration is computationally demanding, and so we expect it to be used only when high-resolution information about intra-floe variability and floe fractures is needed. The basic version of the model does not keep track of the sub-floes and homogenizes floe characteristics after processes like welding.

While convex element shapes lead to dramatic simplifications in calculations of the collision forces, our model allows for concave floes for better realism. Such crucial processes as floe fractures, welding, and ridging are in no way restricted to preserving the convex nature of the floes. In addition, creating new floes in complex empty areas between existing floes becomes a much simpler task when concave floes are used, allowing an arbitrarily-high concentration to be achieved without substantially modifying the floe-size distribution of existing floes. While the SubZero model can be reduced to a conventional DEM by using fixed-shape convex elements, its ability to simulate complex time-evolving floe shapes provides much more flexibility to enhance the realism of the model output.

In comparison with conventional sea ice DEMs, bonds between floes in the SubZero model play a less critical role, especially in highly-packed winter simulations, as some of their functionality is transferred towards parameterizations of floe fractures and ridging/rafting. In winter-time simulations, wherein our model element shapes are allowed to evolve in time, the model state is composed of highly complex and packed floes interlocked with each other. The interlocking behavior of complex-shaped polygons ensures that they are essentially bonded without having any explicitly prescribed bonds between them. The only plausible way to have relative motion in this system is to generate a set of fracture/ridging/rafting events that could split a sufficient amount of floes from each other, creating some open area to allow motion. As a result, having bonds between floes is not entirely necessary, as their role is transferred to such parameterizations as fractures/ridging/rafting that change the shapes of floes and reduce the sea ice area. Nonetheless, the bonds are necessary for more complex configurations of our model that can resolve dynamics within individual floes by splitting them into bonded sub-floes. Such configurations bring more detail to resolving the stress/strain within the floes, which may be relevant for predicting processes like fractures occurring at a subset of floes in the location of interest, like field camps or ship/submarine paths.

3.2 Creation of new floes algorithm

Two primary scenarios call for the creation of new sea ice floes (also referred to here as 'packing'). First, at the beginning of a run, it is necessary to define the initial state of the floes corresponding to a designated sea ice concentration. Second, new floes will be created to fill the open space around existing floes if required by the thermodynamic criteria. New floes are created by the packing algorithm that requires specifying a target concentration for the entire domain (see an example in Figure 3) or by inputting a 2D matrix that specifies the desired spatially-varying concentration on a specified Eulerian grid.

The packing algorithm is designed in the following way. First, it identifies the space unoccupied by existing floes using polygonal operations like unions and differences. Then, the identified region is broken up into polygons using the Voronoi tessellation (Boots et al., 2009) and ensuring that each added new floe is not overlapped with existing ones by cutting the overlap region if it exists. The Voronoi tessellation partitions the domain into

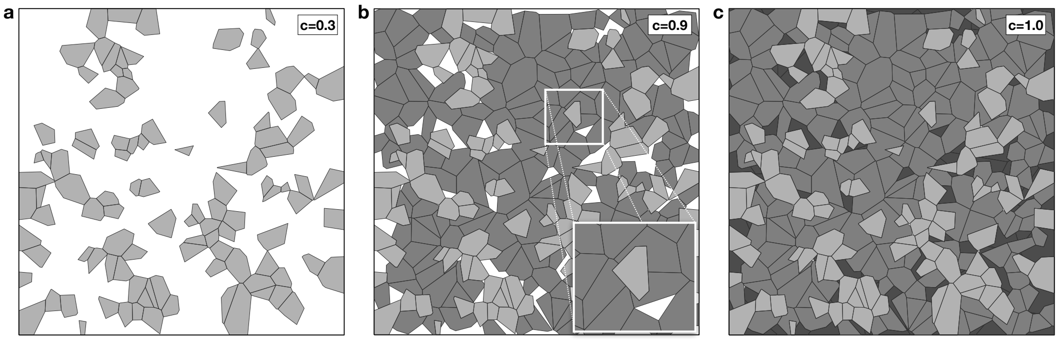

Figure 3. The model's initial state was achieved using the floe packing algorithm that incrementally increases the number of floes to match the desired mean sea ice concentration. Panels **(a-c)** correspond to the initial state at 30% sea ice coverage, floes are added to reach 90% coverage, and then later, more floes are added to reach 100% sea ice coverage. White indicates open ocean, while the newer ice is thinner and is shaded as a darker color. Note that all floes are non-overlapping, and new floes are created in open areas without affecting the old floes. This creates concave floes that are interlocked with other floes, an example of which is shown in the panel **b** inset.

non-overlapping regions (cells) using a set of random seeds (points on a two-dimensional plane). These Voronoi cells become new floes, and are added until a targeted concentration is reached (Figure 3b and Figure 3c). Control on the characteristic sizes of the floes exists by prescribing the number of points used for Voronoi tessellation. The new floes are then added to the floe structure that carries all floe parameters. The initialized floe velocities match the ocean velocity. However, the new floe velocity could also be set to zero in most circumstances as the floe velocity has a relatively short adjustment timescale to the external forcing. The packing algorithm is time-consuming and hence is not used at every time step but with a specified frequency. The thickness of newly created floes follows Stefan's law for ice growth (Leppäranta, 1993) and is related to the time separation between packing events and on the heat fluxes received by the sea ice (Cox & Weeks, 1988):

$$h_0 = \sqrt{\frac{2\varkappa \Delta t N_{pack}(T_o - T_a)}{\rho_{ice} L}}, \tag{1}$$

where $\varkappa$ is the thermal conductivity of the surface ice layer, Δt is the time step during a model run, N_{pack} is the time steps between floe creation events, L is the latent heat of freezing and has units of Joules per kilogram, T_a is the temperature at the ice/air interface, and T_o and is the temperature at the ice/ocean interface. The values used in SubZero are provided in Table 2 and Table 3. We note that snow has a different conductivity from sea ice, but it isn't present in the current version of SubZero. Nonetheless, adding a snow model to SubZero would be straightforward, and we envision doing so in the future, at a stage of implementing two-way coupling with an atmospheric and oceanic model.

3.3 Floe momentum and angular momentum evolution

Each floe in the model is treated as a rigid body with its center of mass $\mathbf{X}_i$ accelerating due to internal and external forces. At the same time, its angular velocity Ω_i responds to the torques:

$$
\begin{aligned}
m_i \ddot{\mathbf{X}}_i &= \iint_{A_i} (\tau_{\mathbf{ocn}} + \tau_{\mathbf{atm}})\, dA + \sum_{j \neq i; k} \mathbf{F}_{ij}^k + \bar{\mathbf{f}}_i, \\
I_i \dot{\Omega}_i &= \iint_{A_i} (\mathbf{r} - \mathbf{X}_i) \times (\tau_{\mathbf{ocn}} + \tau_{\mathbf{atm}})\, dA + \sum_{j \neq i; k} (\mathbf{R}_{ij}^k - \mathbf{X}_i) \times \mathbf{F}_{ij}^k + \bar{g}_i.
\end{aligned}
\tag{2}
$$

Here, indices i and j denote different floes and k enumerates their contact points as several of those could exist for concave floes; m_i, I_i, A_i are floe mass, moment of inertia (Marin, 1984), and area; $\mathbf{r}$ is the location of all points within a floe being integrated over; $\tau_{\mathbf{ocn}}$ and $\tau_{\mathbf{atm}}$ represent kinematic stresses from ocean and atmosphere; $\mathbf{F}_{ij}^k$ and $\mathbf{R}_{ij}^k$ are the interaction forces and coordinates of the k^{th} contact point for colliding i^{th} and j^{th} floes (land is conveniently treated as a stationary floe); and $\bar{\mathbf{f}}_i, \bar{g}_i$ are average forces and torques due to interactions with small-scale floes, that are unresolved owing to the floe-size truncation. An Adams-Bashforth two-step method is used to time-step the model when calculating the trajectories of each floe. A constant time-step is currently used in this prototype version of the model, but an adaptive time-stepping algorithm will be implemented in future versions. A description of the kinematic stresses from the ocean and atmosphere calculations is provided in section 6. Other body forces, such as the Coriolis and sea surface tilt forces, can be turned on. In addition to shape-conserving interactions, the model includes a criterion for floe mergers (welding), ridging, as well as fractures leading to the creation of new smaller floes. Like continuous sea-ice models, the floe model is also limited in its effective resolution by imposing the minimum floe size threshold parameter to bound the total number of elements. This minimum floe size is a parameter that could vary depending on the type of sea ice in a given region, the physical problem under consideration, and available computing resources. For simplicity, and given the lack of developed parameterizations, the basic version of the model does not include the forces and torques from unresolved floes (so $\bar{f}_i = \bar{g}_i = 0$), but later versions would include stochastic representations of the impact of unresolved floes on the dynamics of the resolved floes.

3.4 Contact forces between the floes

3.4.1 Detection of contact points

Each floe has a bounding circle associated with it, with the radius corresponding to the distance from its center of mass to the furthest vertex of its boundary (Figure 4). The bounding floe radii are then used to identify pairs of floes that could be potentially interacting. The polygons of the potentially interacting floes are copied into the memory for each of the floes to enable parallel computation of more complex polygonal operations to determine if the floes are actually overlapping and calculate the collision forces. Note that the floes are considered rigid (non-deformable) bodies, but we allow a small numerical overlap between the floes to exist in order to compute collision forces that depend on the geometry of the overlap area, as common with soft-body discrete element methods (Cundall & Strack, 1979; Luding, 2008; Radjai & Dubois, 2011). Collision forces, $\mathbf{F}_{ij}$, consist of elastic (normal) and frictional (tangential) components which correspondingly are directed along and perpendicular to the line of contact between the two floes.

3.4.2 The normal direction at a contact point

The desired capability of simulating collisions between complex-shaped floe translates into some ambiguity in defining the normal and tangential directions at the contact points, which isn't present for simple convex shapes like circles. For concave polygons, two issues need to be addressed. First, there can be multiple contact points between two concave floes (see an example in Figure 4), and the forces associated with each need to be resolved separately. Second, when sufficiently large forces are driving the floes, the overlap area in some contact points can be of very complex shape such that it isn't

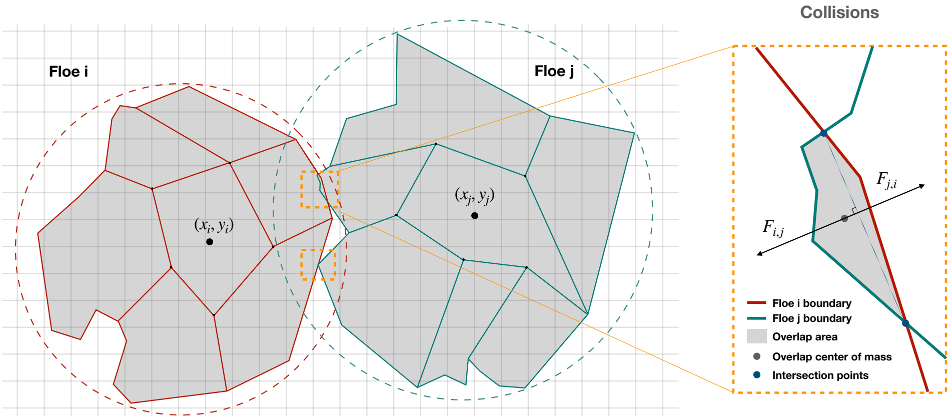

Figure 4. Example of two colliding floes outlining the corresponding normal collision forces appearing at the overlap areas. The bounding circles are shown for both floes and are used to determine if any two floes could be potentially colliding. Each floe could be composed of several rigidly-connected polygonal sub-floes if a more accurate floe-fracture model is needed. An example Eulerian grid that can be used for coupling with the oceanic and atmospheric model is shown with gray lines.

clear how to define the directions of the collision forces. Here, we define the normal direction motivated by Feng et al. (2012). First, at each contact point, the floe polygons intersect each other at two points, and we store the mid-point between them. Second, we calculate the center-of-mass position of the overlap area. The normal force is defined as pointing from the center of mass of the overlap area towards the mid-point of the polygon intersections. Finally, a check is made to ensure the overlap area would be reduced if the floes are displaced in the direction of the corresponding normal forces; the normal direction is flipped if the check fails, which occurs in rare marginal cases with complex shapes of the overlap areas.

3.4.3 Normal forces

For each pair of interacting floes, an algorithm is used to determine the geometry of the overlapped area and the corresponding forces and torques. An energy-conserving contact algorithm (Feng et al., 2012) is used. The floe collision rules are based on simple physical laws for inelastic collisions of rigid bodies (Hopkins et al., 2004; Kulchitsky et al., 2017; Wilchinsky et al., 2010). The normal forces depend on the relative location of the floes, being proportional to the overlap area at each contact location and the proportionality constant $\mathcal{K}$. For a given interaction force, increasing the parameter $\mathcal{K}$ decreases the overlap area between the floes to the extent that they start to appear like rigid bodies; however, this occurs at the expense of having to use a relatively small time interval to accurately resolve the collision forces. The parameter $\mathcal{K}$ could be taken to be as large as possible depending on the computational capabilities and the desired accuracy of collisions. However, keeping it finite brings a physical meaning that the floes are elastic and could have deformation expressed in the form of a finite overlap region between the flow and a general decrease of the overall area in the domain under compression. The equation for the normal force between the i^{th} and j^{th} floes at the k^{th} contact point, $\mathbf{F}^k_{ij,n}$, is given as

$$\mathbf{F}^k_{ij,n} = \mathcal{K}\mathcal{A}\mathbf{n}^k_{ij}, \tag{3}$$

where $\mathcal{A}^k$ is the overlap area and $\mathbf{n}^k_{ij}$ is the normal direction at the k^{th} contact point between the i^{th} and j^{th} floes. Note that for concave elements, there could be multiple contact points, and hence k could be greater than one. The elastic component is similar to a simple linear spring so an effective stiffness $\mathcal{K}$ can be found through the the equation for springs in a series

$$\mathcal{K} = \frac{E_i h_i E_j h_j}{E_i h_i r_j + E_j h_j r_i}, \tag{4}$$

where E is an elasticity value, h is the thickness, and r quantifies the floe size. The floe size is defined to be r_i, which is the square root of the area of the i^{th} floe. Note that smaller floes have higher effective stiffness, requiring smaller time steps to resolve their collisions. The values used in SubZero are provided in Table 2 and Table 3. If there is an individual floe interacting with a non-deformable boundary ($E_j \to \infty$) then the equation simplifies to

$$\mathcal{K} = \frac{E_i h_i}{r_i}. \tag{5}$$

3.4.4 Tangential forces

Discrete element models with bonds commonly utilize force-displacement laws for viscous-frictional tangential forces (Cundall & Strack, 1979; Hopkins et al., 2004; Herman, 2016; Damsgaard et al., 2018). For this model, which does not have bonds, the frictional tangential force is associated with the average tangential velocity difference between the floes at the contact location (Chen et al., 2021). The basic frictional force model defines a coefficient of static friction and a smaller coefficient for kinetic friction, taking the force to be proportional to the normal force only.

When the floes are in motion, the adjustment for the frictional laws is proportional to the velocity difference between the two floes, the time step, and the chord length c^k_{ij}. The chord length is defined as the distance between the interaction points (Figure 4). The equation for the tangential force between the i^{th} and j^{th} floes at the k^{th} contact point, $\mathbf{F}^k_{ij,t}$, is given as

$$\mathbf{F}^k_{ij,t} = c^k_{ij} G v^k_{ij} (\Delta t) |\mathbf{F}^k_{ij,n}| \mathbf{t}^k_{ij}, \tag{6}$$

where G is the shear modulus, velocity v^k_{ij} gives the difference between the two floes, and $\mathbf{t}^k_{ij}$ is the tangential direction at the k^{th} contact point between the i^{th} and j^{th} floes. The values used in SubZero are provided in Table 2 and Table 3. The velocity v^k_{ij} is given by

$$v^k_{ij} = \left[\left(\mathbf{v}_j + \omega_j \times \mathbf{r}^k_j\right) - \left(\mathbf{v}_i + \omega_i \times \mathbf{r}^k_i\right)\right] \cdot \mathbf{t}^k_{ij}, \tag{7}$$

where r^k_{ij} is the position vector of that contact point from the center of mass of the i^{th} floe to the contact point at the k^{th} contact point; $\mathbf{v}_i$, ω_i are the linear and angular velocity of the i^{th} floe at center of mass. However, per friction laws the tangential force is limited by a proportionality to the coefficient of friction (μ) and magnitude of the normal force (Cundall & Strack, 1979; Hopkins, 1996) such that

$$\mathbf{F}^k_{ij,t} \leq \mu |\mathbf{F}^k_{ij,n}| \mathbf{t}^k_{ij}. \tag{8}$$

The presence of tangential forces leads to energy dissipation upon collisions.

3.5 Interactions with boundaries

Coastal boundaries are naturally prescribed as stationary polygonal floes, and an arbitrary number of such boundaries (defined to be the value N_b in Table 2 and Table 3) are possible if, for example, one is interested in simulating the sea ice in Fjords with many islands. The interaction forces with the coastal boundaries are calculated in a similar way as with other floes, but assuming that the elasticity of a boundary is infinite (i.e. all elastic deformation occurs within a floe). The frictional parameters with coastal boundaries could be different, although they are kept the same by default. Periodic boundary conditions could be used in addition to coastal boundaries in channel-type configurations. Periodic (and double-periodic) boundary conditions are achieved by using ghost floes. The ghost floes are shifted copies of all floes that are close to one boundary and have the potential to overlap with the floes at the other boundary. The framework dealing with periodic boundary conditions is also directly applicable for parallel implementation as each processor could resolve its sub-domain in physical space and exchange the information about the location of ghost floes at its edges with neighboring processors. This capability will be implemented in future versions of the code, but in its current form, parallel computing is utilized by cores within a single node with Matlab's "parfor" loops.

4 Processes affecting floe shapes

4.1 Floe fractures

4.1.1 Defining the floe stress tensor

Stress and strain rates are important for physical processes such as fracture and lead formation. The collision function keeps track of the location and forces associated with each collision. We treat the stress as being homogeneous across individual floes and calculate the stress tensor ($\underline{\underline{\sigma_i}}$) of individual floes (Rothenburg & Selvadurai, 1981; André et al., 2013) via

$$\underline{\underline{\sigma_i}} = \frac{1}{2\mathcal{V}_i} \sum_{j,k} f^k_{ij} \otimes r^k_{ij} + r^k_{ij} \otimes f^k_{ij}, \tag{9}$$

where $\mathcal{V}_i$ is the volume of the i^{th} floe, f^k_{ij} is the force at the k^{th} contact point between the i^{th} and j^{th} floes and r_{ij} is the position vector of that contact point from the center of mass of the i^{th} floe to the contact point. The stress tensor is later used to define the floe fracture criteria. The continuous representation of the stress tensor over a coarse Eulerian grid (see section 6.2) is obtained by volume-weighted averaging of the stress tensors of the individual floes (Chang, 1988) within each grid box:

$$\underline{\underline{\sigma}}(x, y) = \frac{1}{\mathcal{V}_{tot}} \sum_i \underline{\underline{\sigma_i}} \mathcal{V}_i, \tag{10}$$

where the index i includes only floes with centers of mass located inside the coarse grid box at the location (x, y) and $\mathcal{V}_{tot}$ is the total volume those floes excluding the floe areas outside the grid box.

4.1.2 Fracture criteria based on homogenized floe stress

The homogenized stresses are used in the following way, depending on the configuration of model parameterizations. The main usage revolves around defining the appropriate criteria for fracturing individual floes based on local and/or non-local stress criteria. Specifically, it is straightforward to define fracture criteria based on, e.g., Mohr-Coulomb failure envelope (Figure 5) that is defined in the space of principal stresses of a floe stress tensor (Weiss & Schulson, 2009). The equation for the failure envelope boundaries are $\sigma_1 = q\sigma_2 + \sigma_c$ where $q = 5.2$ and $\sigma_c = 250$kPa. Here σ_1 is the associated maximum principal stress and σ_2 is the intermediate principal stress. Other options for floe-fracture criteria could be derived from yield curves that are used in continuous models (Hibler, 1979). The connection with the SubZero model, where floes are rigid (non-deformable) objects, is that the macro-scale strain rate appears when floes are fracturing (or ridging/rafting). Thus, satisfying criteria for individual floe fractures would lead to macro-scale sea ice motion, which in continuous formulations is described by the presence of a yield curve. For example, in viscous-plastic sea ice rheology, an elliptical yield curve is used with a strength parameter (P) where $P = P^*h$ that is proportional to sea ice thickness h for fully ice-covered regions (Hibler, 1979). The values of P^* is a fixed empirical constant and the value used in SubZero are provided in Table 2 and Table 3.

The basic isotropic fracture mechanism is implemented based on the stress experienced by floes and fractures a floe into a number of smaller pieces (Figure 6) when the principal stress values satisfy the specified fracture criteria (Figure 5). When it is determined that a fracture should occur, a floe is split into the desired number of elements via Voronoi tessellation based on random x and y points coordinates (uniform distribution) acting as centers of the Voronoi cells. The mass, momentum, and angular momentum are conserved after the floe fractures into smaller pieces.

The number of elements into which the floe splits can be determined via a probabilistic process based on the proximity of the floe stress to the boundaries of the failure criteria or simply preset at a fixed number (e.g., $N_{Pieces} = 3$) as we did in our idealized model configurations (Table 2, 3). The shattered pieces form new floes that could continue breaking until stresses are relieved. This is a simple procedure leading to an isotropic distribution of fractures regardless of the direction of the principal stresses. Note, without fracturing, the packed and interlocked floes would have no motion, and hence the movement occurs when the particle fracture criteria are satisfied. Therefore, one could draw connections between the concepts of the yield curve in continuum mechanics and the fracture criteria of the elements, but those would need to be constrained with floe-scale observations.

The basic fracture criteria implemented in the model include the Mohr's cone and the elliptical yield curve used in viscous-plastic rheology (Figure 5). Any other breakage criteria could be easily implemented. For studies focusing on the analysis of linear kinematic features, it would be necessary to formulate more advanced floe fracture criteria or use bonds between floes to explicitly simulate fracture formation. This is an ongoing area of model development, and we envision enabling this capability in future versions of SubZero.

4.1.3 Corner grinding

Observations of older floe fields show a tendency to form rounder shapes through repeated interactions with other floes. The corner grinding process uses the contact overlap areas to determine whether a floe could have its corner fractured; the likelihood of this happening is proportional to OverlapArea/FloeArea. The model tracks the contact points during a collision with other floes, and if there is a contact point nearby, it is qualified to fracture. The properties of the new floes are calculated to satisfy mass, momentum, and angular momentum conservation laws. For a corner with interior angle α and

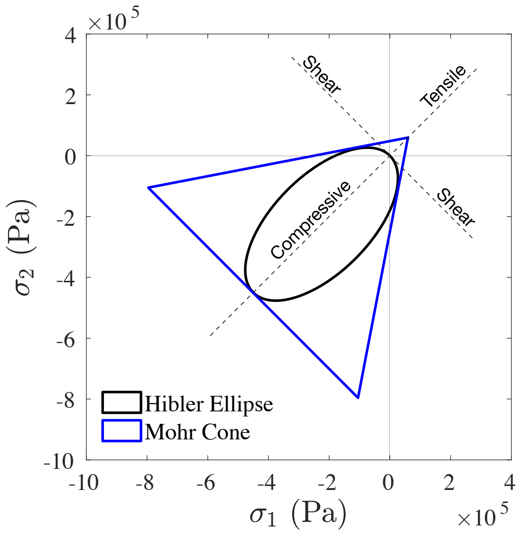

Figure 5. Examples of fracture criteria plotted as boundaries in the (σ_1, σ_2) principal stress space, including Mohr's cone and Hibler's ellipse. Floes for which homogenized stresses are large enough to reach (or temporarily exceed) the fracture criteria boundaries end up fracturing into several elements. Those boundaries could be interpreted as yield curves for individual floes because only upon reaching those boundaries can there be any motion within the floe by means of fracturing it into smaller pieces.

adjacent sides of length l_1 and l_2, where $l = \min(l_1, l_2)$ (Figure 7a), at least one contact must be within the radius l of the corner. For each eligible corner of the polygon, a fracture probability is defined as 1-α/Anorm, where Anorm=360-180/N, and N is the total number of vertices. This way, the probability of fracture increases as α approaches 0^o. For all floe corners that fracture, a triangle is defined with the same angle α and adjacent edges five times smaller than l. Figure 7 shows a floe field going through the corner fracture process. It can be seen that some of the sharper corners are broken off from 7a as the angles trend closer to that of a regular polygon. Figure 7b shows the rounded floes after many collisions, and the fractured pieces have been plotted with a dark gray color to distinguish them from the initial floes (colored with light gray).

4.2 Welding

It is common for two ice floes to weld together when the temperature dips below freezing over the winter in the arctic. We define welding as the freezing of neighboring ice floes to form a bigger consolidated floe (Figure 6). We model this process by using thermodynamic criteria to determine if two overlapping floes will weld together. When welding occurs, the properties of the newly created floe are determined by satisfying the mass, momentum, and angular momentum conservation laws. Our most straightforward parameterization defines the welding probability (P^i_{weld})of a floe in contact with another floe as

$$P^i_{weld} = P_{F^i_{heat}} \frac{\delta A_{i,j}}{A^i} \tag{11}$$

where $\delta A_{i,j}$ is the overlap area between two floes, and the proportionality constant $P_{F^i_{heat}}$ is non-zero only when the ice is freezing. Improvements to this simple process could spec-

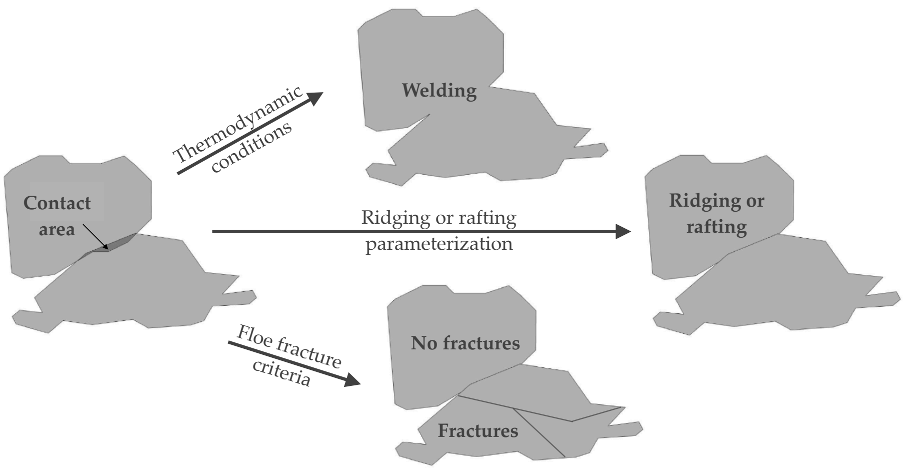

Figure 6. Example of two floes in contact leading to various possible outcomes, including welding, ridging/rafting, and fractures. The floe interaction forces are computed based on the geometry of the overlapping area. Collision forces define the homogenized floe stress tensor used in the fracture parameterization that splits the floe into several pieces. Welding occurs if a thermodynamic criterion is satisfied and leads to the merger of two floes into one. The ridging/rafting parameterization determines if the overlap area between the floes will be absorbed into increasing the thickness of one of the two floes in contact.

ify the probability to depend on the heat flux out of the ice floe or duration of the contact (Shen & Ackley, 1991).

4.3 Ridging and rafting

Upon contact with other floes, a sea ice floe can either become thicker or transfer some of its mass to another floe through the ridging process. For this model, we implemented a simple parameterization based on a critical thickness that is set to determine if ridging or rafting is possible for two floes in contact (Parmerter, 1975). Additionally, a probability for ridging (P_{ridge}) is defined so that only a subset of floes will undergo the ridging process. For the current version, it is set to a simple percentage value, and if at least one of the floes exceeds this threshold, then ridging will take place. However, more complex probabilities can depend upon compressive stress and thickness (Hibler III, 1980; Hopkins, 1998; Hopkins et al., 1999; Tuhkuri & Lensu, 2002; Damsgaard et al., 2021). When ridging occurs, the area of the floes is reduced as the mass is transferred toward increasing the thickness of one of the colliding floes. If both floes exceed the critical thickness ($h_c = 0.25$), a probability function (P_{Floei}) is set to determine the exchange of mass between the two floes, where the probability that the mass moves from floe i to floe j is

$$P_{Floe^i} = \frac{1}{1 + h_i/h_j}, \tag{12}$$

where h_i and h_j are the thicknesses of the two floes undergoing ridging. If only one floe exceeds the thickness, then the thin floe loses its mass to the thicker floe. Floe properties are updated to ensure that the overall mass and momentum are conserved upon the adjustment of floe shapes (Figure 6). The ridging of sea ice can lead to complex sea ice

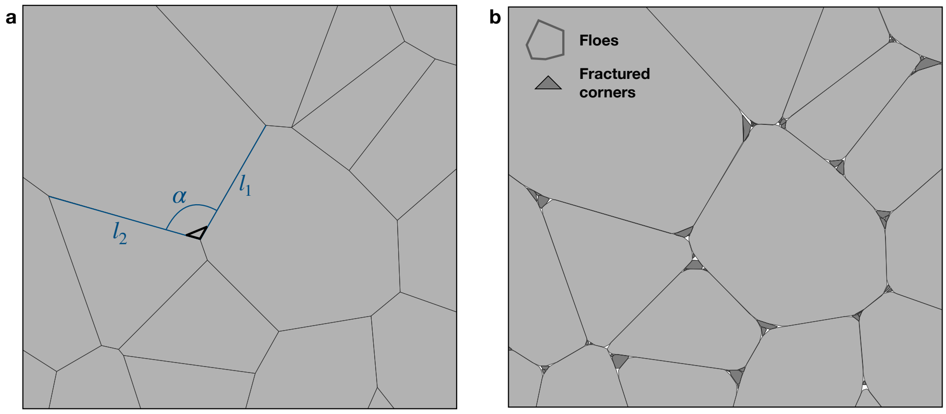

Figure 7. Example of floes where the sharp corners are breaking off upon tight contact with other floes. **(a)** The initial intact floe configuration with fully-packed interacting floes. Denoted are an interior angle, α, the lengths of adjacent edges, l_1 and l_2 . The black line denotes the corner that will be fractured (isosceles triangle with the same angle α). **(b)** The state of the floes after the occurrence of multiple corner fractures. Fractured corners are modeled the same as regular floes, but here they have been plotted with a dark gray color to distinguish from the initial floes that are colored with light gray.

shapes with a computationally prohibitive number of vertices. To reduce their complexity, we implement an algorithm that dynamically simplifies floe shapes (see Section 5.2).

When the two interacting floes are both below this critical thickness threshold, h_c, they have a possibility of rafting where P_{raft} is a value set by the user. The numerical algorithm for the rafting process is similar to ridging, and mass will transfer from one floe to the other. After this rafting event, the floe that loses mass will also have its area updated. Floe properties are updated to ensure that mass, momentum, and angular momentum are conserved throughout this operation. The updating of floe geometry is also similar to that shown in Figure 4.

4.4 Thermodynamic thickness changes

For existing floes a Semtner 0-layer approach is taken (Semtner Jr, 1976). The basic version of the thermodynamic sea ice growth calculates the tendency of its thickness based on the net atmospheric and oceanic heat fluxes, and the tendency is inversely proportional to its thickness. This thickness growth assumes that the temperature inside the sea ice is always equilibrated to a linear profile, and the changing thickness is the only variable governing the heat flux. This basic version of the code is aimed at simulating sea ice mechanics, and hence the thermodynamic processes are simplified. Future thermodynamic schemes will include the option of using multi-layer thermodynamics and include the treatment of snow cover. For small-scale floes (about 100 m and smaller), lateral growth and melting can be important, and this capability will also be implemented in future versions of the code.

In open-ocean regions where there are no ice floes, and freezing conditions are satisfied such that the surface ocean temperature is maintained at the freezing point, the lost heat fluxes are partitioned into creating new floes with a prescribed minimum thickness. Thus, the total volume of new floes to be created in an open area, together with the minimum floe thickness, defines the total area of the new floes that are then generated using the packing algorithm.

5 Peculiarities of the numerical implementation

5.1 Tracking unresolved floes

Keeping track of all the small floes generated through the fracturing and ridging processes performed in the model becomes computationally expensive. This expense comes from both an increased particle count and shorter time steps associated with the higher elasticity in small floes. Thus, a lower limit is set, at which point any floe with a smaller area is removed from the simulation and kept track of in a separate variable. The mass of all unresolved floes is stored in a variable on a coarse Eulerian grid. Utilizing the Eulerian sea ice velocity (see section 6.2), the dissolved ice mass is advected around the domain to preserve mass. Under proper thermodynamic conditions, this unresolved floe variable can act as a source for newly generated floes via section 3.2, conserving the mass of the system. In future versions of the model, parameterizations of the cumulative dynamical impact of small-scale unresolved sea ice will be used in the calculation of forces and torques on the remaining floes.

5.2 Dynamic simplification of floe boundaries

Figure 8. Example of a boundary simplification for a polygonal floe using the Douglas-Peucker algorithm. Initial floe boundary with 292 vertices (blue), its moderate simplification to 81 vertices (red), and heavy simplification to only 23 vertices (black). Inset shows a zoomed-in view of the protruding region at the top of the floe inside a black square box.

Repeated application of certain processes in the numerical implementation (such as ridging, welding, and floe creation) can lead to floes with a very large number of vertices, which is problematic for two reasons. First, running simulations with large numbers of floes create excessively large data structures that need to be stored. Secondly, performing operations such as rotating, translating, or calculating overlaps with other floes becomes computationally cumbersome. To avoid this, we periodically check the number of vertices and, when appropriate, apply a Douglas-Peucker simplification algorithm to reduce the complexity of the shape. The floes retain qualitatively similar shapes as shown in Figure 8. After its simplification, the thickness of the floe is updated to conserve mass and momentum.

5.3 Parallel for-loops for multi-core processors

The SubZero program can run the collision algorithm, update floe trajectories, create new floe elements, weld floes, and fracture floes in parallel. To achieve this, we define for each given floe the potential interactions field that essentially copies all the necessary information about only those surrounding floes that have their bounding circles overlapping with a given floe. The potential interactions are found as described in section 3.4. The floe number, vertices, velocities, thickness, area, and centroid are all stored. This data is required to calculate the collisions between two floes and when two overlapping floes weld together independently of other rows in the floe structure. Updating floe trajectories and fracturing floes can be done in parallel and do not rely upon information from other floes in the structure. The creation of new elements and the welding algorithm divides the domain into smaller regions and bin the ice floes based on location. These subregions are then run in parallel.

6 Coupling with ocean and atmosphere models on the Eulerian grid

6.1 Atmosphere and ocean forcing of individual floes

The atmospheric and oceanic equations of motion could be solved either within the Eulerian or Lagrangian frameworks, although typical climate models are Eulerian. We hence provide the coupling capability with the floe model based upon the gridded (Eulerian) representation of sea ice variables. For calculating the oceanic and atmospheric forces and torques acting on individual floes, a Monte-Carlo method (Caflisch, 1998) is used for the integration of stresses over the surface areas of the floes. The Monte-Carlo integration method uses random sampling of the desired function to numerically estimate the integral. The integral of the desired function is approximated by averaging samples of the function at random points over the surface, while typical algorithms evaluate the integral on a regularly spaced grid. For this model, random points in space are assigned, and ocean and atmosphere flows are interpolated onto these points, after which stresses are computed. Less than about 100 points are needed for an accurate estimation of stresses, resulting in about 5% accuracy (Oberle, 2015). The surface stresses as well as salt and heat fluxes that the ocean model receives from the sea ice model are computed by taking averages of the floe stresses and growth/melt rates over an Eulerian grid of the ocean model. This achieves a two-way coupling of both dynamic and thermodynamic components of the ocean and ice models. The same coupling can be arranged with the atmospheric model, and this capability would be implemented in the code as part of future developments.

6.2 Mapping the state of the floe model to the Eulerian grid

A coarse Eulerian grid is designated for the domain to diagnose the macroscale motion of the sea ice and couple it with Eulerian oceanic and atmospheric models. The domain is divided into smaller regions that align with this coarse spatial grid shown by the black lines (Figure 9). Floes that overlap with any piece of the subregion are identified, and the concentration is calculated first. Next, variables such as sea ice velocity and acceleration are calculated by scaling the contribution of individual floes by the mass of a floe present within the cell in question. Other variables, such as the total force exerted on a coarse grid cell, are not weighted by the mass of the floe experiencing the force.

7 Examples of simulated sea ice behavior

Here we present several test cases demonstrating the potential utility of the SubZero sea ice model. Specifically, we showcase simulations that highlight the specific physics of the model, including the role of floe fractures in a pure compression experiment, the

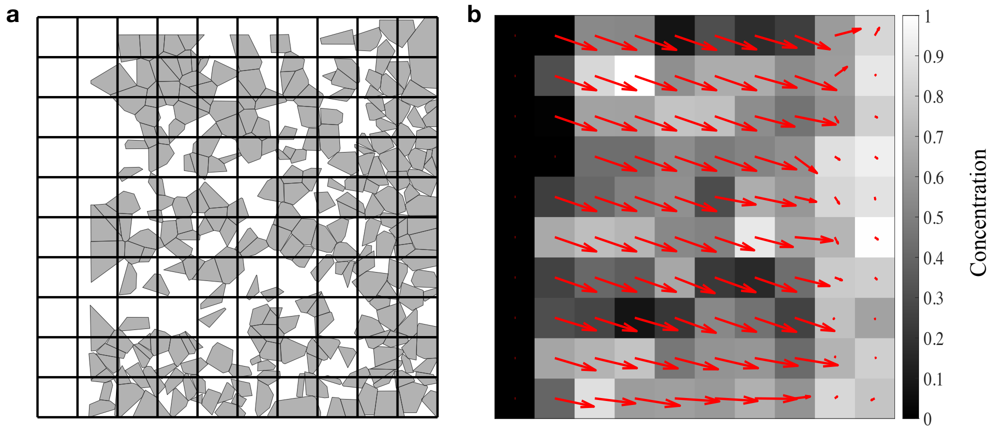

Figure 9. Example of a coarse graining including **(a)** a set of floes with total 50% concentration mapping the state of the floe model to the Eulerian grid where the domain is split into 10x10 grid with stationary solid boundaries. The ocean is stationary and the winds are blowing at 10m/s from left to right. **(b)** The homogenized values of floes plotted on the coarse Eulerian grid with shading indicating the concentration within the subregion and the arrows indicating the coarse sea ice velocity with a maximum velocity of 0.2m/s.

evolution of floe size distribution in a domain with a complex coastline, and the wintertime simulation that includes all model physics.

7.1 Evolution of sea ice floes under uniaxial compression

The behavior of granular-type materials, including sea ice, is commonly tested using idealized deformation experiments, e.g., subjecting the material to externally-imposed pure compression (Figure 10), tension, or shear. Here we demonstrate the behavior of sea ice floes subject to uniaxial compression in a confined domain, which is just one of the possible experiments that illustrates the non-standard formulation of the SubZero model. Each run is initialized with 200 floes in a fully-packed domain (Figure 10a), the North/South boundaries moving towards the center of the domain, and stationary East/West boundaries. A relatively small time step, dt=5 s, is used to resolve the elastic waves in response to external boundary motion and changes in the floe configuration due to fractures. The atmospheric and oceanic stresses are set to zero for this simplified test. The floes are subject to Mohr-Coulomb fracture criteria ($N_{frac} = 100$), but there is no floe simplification, corner grinding, welding, ridging, rafting, or creation of new floes in this scenario. The boundaries move with a constant prescribed velocity, $v_b = 0.1$ m s^{-1}, and this leads to an initial increase in the numbers of floes (Figure 10c) and a reduction of the sea ice area when small floes are removed (minimum floe size allowed is 4 km^2) and ensures convergent sea ice motion (Figure 10b). The scenario is run for a range of three different Young's moduli, $E = (5\times10^7, 10^8, 1.5\times10^8)$ Pa, with the temporal evolution of the maximum normal stress averaged over an entire domain shown in Figure 10d. This experimental setup is included in the Zenodo repository (Montemuro & Manucharyan, 2022).

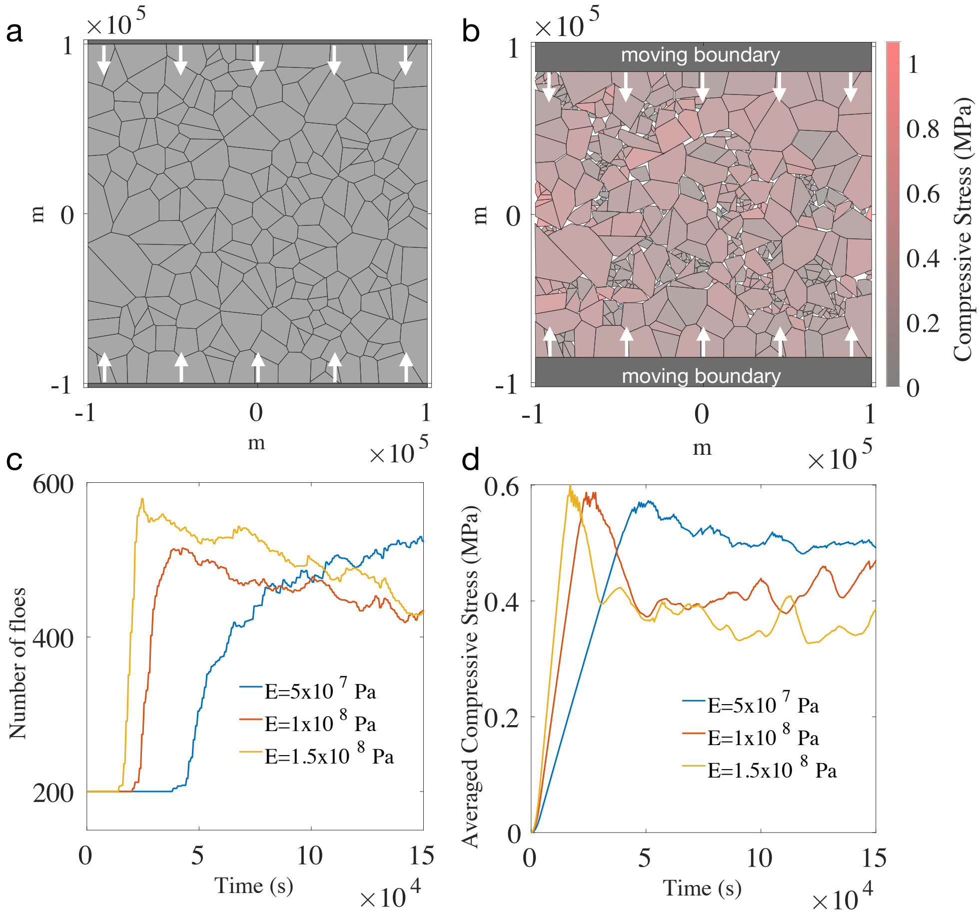

Figure 10. Evolution of sea ice under an idealized compression experiment. **(a)** The state of the floes at the beginning of the simulation for all three compression experiments. White arrows represent the imposed direction of motion of the top and bottom boundaries of the domain; the left and right boundaries remain stationary. **(b)** The state of the floes at the end of the simulation with a reference value of Young's modulus of E=1.5 10^8 Pa, corresponding to the yellow curve in panel **(c)** and panel **(d)**. Panel **(c)** shows the evolution of the number of floe elements in the simulation; the three curves represent runs with different Young's moduli, E, prescribed for the floes. **(d)** Temporal evolution of the maximum normal stress averaged over an entire domain; the three curves represent simulations with different Young's moduli, E, prescribed for the floes. The video of the simulation is available as supplementary material.

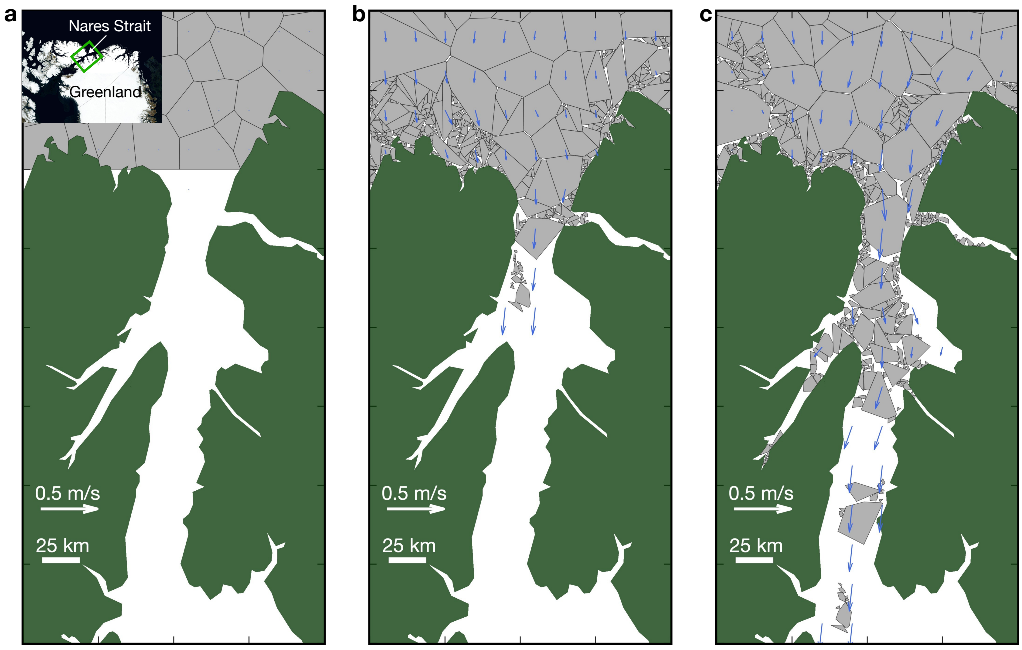

Figure 11. The evolution of sea ice floes as they pass through the Nares Strait, including (a) initial floe state with the inset showing the location of Nares Strait, (b) floes shortly after sea ice breakup that occurred after about three days, and (c) floe state after ten days when many floes have passed through the Nares Strait. The initial distribution of floes was generated using Voronoi tessellation, and the subsequent evolution of floe shapes is only subject to floe fractures. The green box in (a) shows the part of Nares Strait being simulated. The blue arrows represent sea ice velocity after averaging floe momentum on an Eulerian grid. The video of the simulation is available as supplementary material.

Table 2. A list of key parameters used in the SubZero model Nares Strait simulation, including their default numerical values, a brief description, and the processes that use these parameters.

Parameter	Description	Process
$E = 5 \times 10^7$ Pa	Young's Modulus	Floe Interactions
$G = \frac{E}{2(1+\nu)}$	Shear Modulus	
$\nu = 0.3$	Poisson's ratio	
$\mu = 0.25$	Coefficient of Friction	
N_{Frac}=150	Time steps between fracturing	Floe Fractures
$N_{Pieces} = 3$	Number of pieces for fracturing	
$P^* = 1{\times}10^5$ N m^{-1}	Floe strength-to-thickness ratio	
$\rho_i = 920$ kg m^{-3}	Density of ice	Floe mass and moment of inertia
$\rho_a = 1.2$ kg m^{-3}	Density of air	Surface stresses
$\rho_o = 1027$ kg m^{-3}	Density of ocean	
$Cd_{atm} = 10^{-3}$	Atmosphere-ice drag coefficient	
$Cd_{ocn} = 3{\times}10^{-3}$	Ocean-ice drag coefficient	
$N_{MC} = 100$	Number of sample points for Monte Carlo integration over floe surface	
$\Delta t = 10$ s	Integration time step	Time-stepping
A_{min}= 2 km^2	Minimum area of resolved floes	Floe state
$N_b = 18$	Number of floes creating the boundary	

7.2 Summer sea ice motion through Nares Strait

The Nares Strait simulation demonstrates the role of floe fractures in wind-driven sea ice transport through narrow straits. Nares Strait is a channel between Ellesmere Island (Canada) and Greenland (Figure 11a). The simulation aims to reflect spring or summer-like conditions of Arctic sea ice export through Nares Strait after the breakup of its winter arches (Figure 11). Due to floe jamming as they pass through the narrow constriction, the sea ice transport through the strait occurs in the form of episodic events (Kwok et al., 2010; Moore et al., 2021). Since the transport events are relatively short (order of days or less), the effects of thermodynamic sea ice melt could be considered secondary relative to mechanical floe processes such as collisions and fractures. We thus randomly initialize the model with relatively large floes of uniform thickness, covering only the area just north of the strait (see Table 2 for the list of parameters used in this simulation). The uniform 10 m/s southward winds generate stresses that push the floes through the strait, while the ocean is assumed to be stagnant. Coastal boundaries are prescribed using a series of $N_b = 18$ static floes. All physical processes except collisions and fractures are turned off to model the spring/summer breakup of floes. To suppress the rapid creation of tiny floes due to frequent fractures, we set up the simulation to resolve only floes with an area greater than 2 km^2. In this basic model formulation, we assume that the unresolved small floes do not significantly affect the dynamics of retained floes, and the model only tracks their mass density using the Eulerian grid to ensure mass conservation. Note that in more complex model formulations, the mass density could be used to parameterize the cumulative effect of small-scale floes on the dynamics of resolved floes. This experimental setup is included in the Zenodo repository (Montemuro & Manucharyan, 2022).

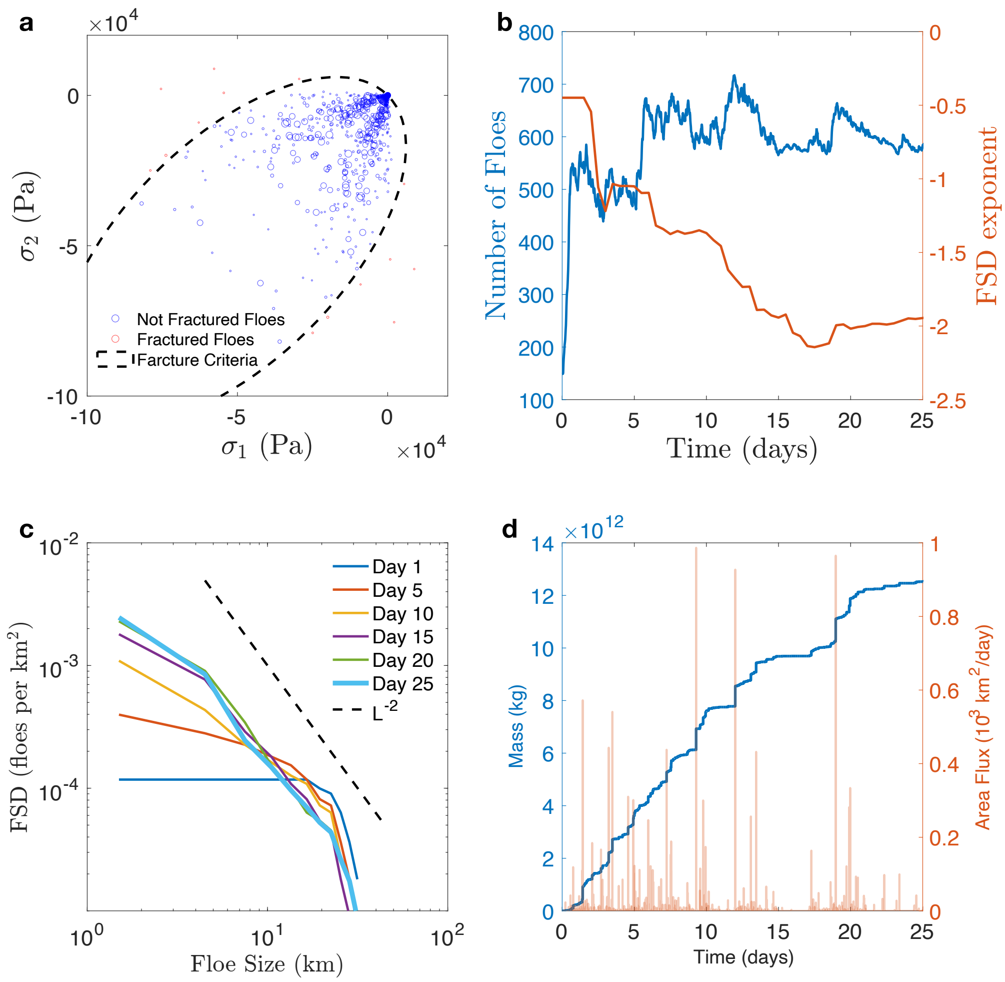

Figure 12. The evolution of the Nares Strait simulation. **(a)** Principal components of the individual floe stresses, with floes categorized by those that will experience fracture (red) and those that will not (blue). The black dashed curve represents a boundary for floe fracturing, an ellipse similar to a yield curve used in viscous-plastic sea ice rheology. **(b)** Temporal evolution of the number of resolved floes (blue) and the FSD exponent (red). **(c)** Floe size distributions for sea ice floes that are inside the Nares Strait. **(d)** The cumulative sea ice mass transport through the northern entrance to the Nares Strait (blue) and the corresponding area flux (red).

As winds push the initially large floes through the strait, the frequent floe fractures lead to an equilibrated floe size distribution (FSD) in just a few weeks (Figure 12b). The number of floes grows from dozens initially to several hundred (Figure 12b), but the FSD takes the form of a power-law distribution with an exponent close to -2 (Figure 12c). The FSD is free to equilibrate to a different power-law exponent (or not be a power law at all) depending on the forcing and floe interaction and fracture laws. In a winter-like simulation described in the next section, the FSD also equilibrates to a power-law distribution but with a different exponent. Power-laws in FSDs have been commonly reported based on observations in various Arctic Ocean regions, with exponents ranging from about -3 to -1 (Rothrock & Thorndike, 1984; Holt & Martin, 2001; Horvat et al., 2019; Denton & Timmermans, 2021). A recent study using very high-resolution images demonstrates that within a wide range of floe sizes, the power-law exponent for the area-based FSD belongs to an approximate range from (-2, -1.65), which translates to a range of slopes (-3, -2.3) if size as the square root of the area is used to define FSD (Denton & Timmermans, 2021). The SubZero simulation with fractures only driven by mechanical floe interactions results in the FSD power law exponent of about -2, which compares reasonably well with observations.

As the sea ice breaks into smaller floes, they can propagate through the relatively narrow strait. The sea ice mass flux through the strait is not smooth as floes often jam in narrow constrictions (Figure 11b). The jamming occurs when relatively large floes cluster in narrow parts of the strait, and sea ice can only move after some of those floes break into smaller pieces. The breaking of floes depends on the fracture criteria; an ellipse was used for this simulation to conceptually mimic Hibler's elliptical yield curve used in continuous viscous-plastic sea-ice models (Figure 12a). Floes with stresses lying inside the ellipse do not break, and those on the ellipse or just outside of it end up fracturing. These floe fractures lead to intermittent but large fluxes of sea ice area and transported mass (Figure 12d). The sea ice area fluxes in Nares Strait estimated using satellite and flux-gate observations are of the order $O(10^3)$ km^2/day (Kwok et al., 2010; Moore et al., 2021) and generally agree with the idealized simulation with $O(10^3)$ km^2/day for relatively rare high-transport events and about $O(10^2)$ km^2/day for more frequent events. Thus, the idealized SubZero experiments can qualitatively simulate many aspects of sea ice dynamics relevant to flow through a narrow channel. However, the parameterization of certain physical processes still requires tuning using floe-scale observations. We expect that observational estimates of FSD and mass fluxes inside Nares Strait and the driving forces, such as wind stress and boundary stresses, would be crucial for constraining floe collision and fracture parameterizations. Winter-time sea ice dynamics in the Nares Strait also present a critical case study since sea ice can form arches that temporarily shut down its transport. This experiment is left for future studies, and we expect that it can be used to tune the balance between welding processes that bond floes together and fractures that break them apart.

7.3 Winter ITD and FSD equilibration

Here we demonstrate an essential case of model equilibration in winter-like conditions, where all parameterizations are active. For a model like SubZero that simulates time-evolving floe shapes and has a freely-evolving number of floes, it is of particular interest to explore if the FSD and ITD equilibrate to distributions resembling observations. We subject sea ice to strong mechanical and thermodynamic forcing over a five week period to facilitate an accelerated model evolution away from the initialized floe shapes, sizes, and thicknesses towards typical winter-like distributions. Specifically, we prescribe idealized ice-ocean stresses in the form of four equal-strength counter-rotating gyres (arranged like mechanical gears, see Figure 13a) that create relative sea ice motion and facilitate floe fractures and ridging. Alternatively, one could prescribe atmosphere-ocean stresses to achieve the same goal, but in this run the winds are set to 0. To make this a winter-like simulation, we ensured a continuous sea ice growth by specifying a fixed

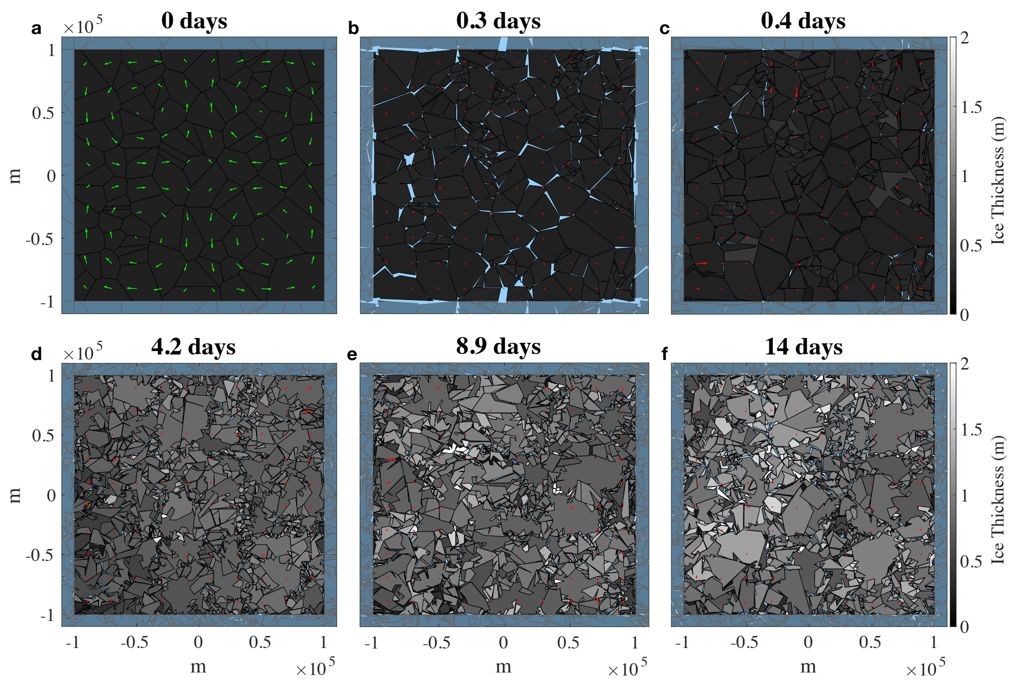

Figure 13. Evolution of sea ice during the winter-like simulation of sea ice growth with full physics of the model enabled. Panels **a-f** correspond to snapshots of floes and their thicknesses (shown with a grayscale color bar) at model times denoted in the panel titles. Panel **a** shows the underlying ocean forcing in green while panels with the maximum ocean velocity being 0.15m/s, and **b-f** show the sea ice velocity in a continuous sense after averaging floe momentum within grid boxes of an Eulerian grid with the red arrows. The video of the simulation is available as supplementary material.

negative heat flux that increases the thickness of existing ice floes, the formation of new ice floes in open ocean regions, and welding between floes (see Figure 2 for the simulation workflow). This idealized setup is aimed to demonstrate the evolution of floe shapes, sizes, and thickness under strong mechanical and thermodynamic forcing. We initialized the model with a fully-packed domain (100 floes) in which floes are cells of the Voronoi tessellation, all having the same thickness of 0.25 m and similar sizes (Figure 13). These initial floe thickness and size distributions are highly unrealistic. Below we describe how the dependence on these initial conditions is lost as the simulation progresses and how the emerging distributions start resembling the observed ones. This experimental setup is included in the Zenodo repository (Montemuro & Manucharyan, 2022).

In the early times of the simulation (within the first days), floe fractures and ridging/rafting processes lead to rapid changes in ITD and FSD (Figure 14). The rates at which these processes occur are given in Table 3. The floe fractures form smaller floes, and this process establishes an approximate power-law distribution in the range of resolved floes, which are larger than a few km. The floe fracture criteria used here again was an ellipse to conceptually mimic Hibler's elliptical yield curve. The ice-free areas open up due to ridging/rafting, and new ice floes are formed there and consequently participate in all processes. Note, the simulation is set to resolve floes with size above a certain threshold, which we set to 2 km^2 for this simulation. After about a week, the power-law exponent of the FSD equilibrates to a value of about -3, and the FSD starts resembling observations. Power laws in FSD are commonly found in various types of satellite sea ice observations, with the -3 exponent being well within the range of reported val-

Table 3. A list of key parameters used in the SubZero model, including their default numerical values, a brief description, and the processes that use these parameters.

Parameter	Description	Process
$E = 6 \times 10^6$ Pa	Young's Modulus	Floe Interactions
$G = \frac{E}{2(1+\nu)}$	Shear Modulus	
$\nu = 0.3$	Poisson's ratio	
$\mu = 0.3$	Coefficient of Friction	
N_{Frac}=75	Time steps between fracturing	Floe Fractures
$N_{Pieces} = 3$	Number of pieces for fracturing	
$P^* = 5{\times}10^3$ N m^{-1}	Floe strength-to-thickness ratio	
N_{cor}=10	Time steps between corner grinding	Corner Grinding
N_{Weld}=25	Time steps between welding	Floe Welding
$P_{F_{heat}}= 150$	Welding probability coefficient	
$P_{ridge} = 0.1$	Ridging probability coefficient	Floe Ridging &
$P_{raft} = 0.1$	Rafting probability coefficient	Floe Rafting
$h_c = 0.25$	Critical thickness for ridging to occur	
$N_{pack} = 5500$	Time steps between floe creation	Floe Creation
$\varkappa = 2.14$ W m^{-1} K^{-1}	Thermal conductivity of surface ice layer	
$L = 2.93 \times 10^5$ J kg^{-1}	Latent heat of freezing	
$N_{simp} = 20$	Time steps between simplification of floe boundaries	Floe Simplification
$\rho_i = 920$ kg m^{-3}	Density of ice	Floe mass and moment of inertia
$\rho_a = 1.2$ kg m^{-3}	Density of air	Surface stresses
$\rho_o = 1027$ kg m^{-3}	Density of ocean	
$Cd_{atm} = 10^{-3}$	Atmosphere-ice drag coefficient	
$Cd_{ocn} = 3{\times}10^{-3}$	Ocean-ice drag coefficient	
$N_{MC} = 100$	Number of sample points for Monte Carlo integration over floe surface	
$\Delta t = 10$ s	Integration time step	Time-stepping
A_{min}= 2 km^2	Minimum area of resolved floes	Floe state
$N_b = 0$	Number of floes creating the boundary	

ues (Rothrock & Thorndike, 1984; Stern et al., 2018). Notably, our model simulation equilibrated to an approximate -3 power law, having only internal sea ice interactions as a cause of fractures. However, in marginal ice zones (regions where FSDs are often computed from observations), floes are also fractured by surface waves (Montiel & Squire, 2017) – a process that is not yet included in our model. Since the inclusion of waves would preferentially create smaller-scale floes, the FSD might have a steeper slope, making the power-law exponent closer to the observations. But before the wave fracture parameterization is included, our simulation can be considered applicable for conditions in pack ice, away from marginal ice zones.

The ITD also departs rapidly from the initial delta function distribution (all floes were initialized with the same thickness). By the end of the first week, the ITD takes the form of a double-peak distribution, with a second peak emerging at around 0.6 m due to ridging processes (Figure 14a). However, as time progresses, the second peak gets smeared out because many different ice thickness categories are ridged with each other. By the end of the month, the ITD takes a form of a smooth, single-peak distribution with a pronounced asymmetric tail for thick ice. The ITD continues to move towards thicker sea ice because of the thermodynamic growth, while the tail of the distribution and its asymmetry increase due to ridging (Figure 14c). At this stage, the dependence on the initially-prescribed ITD shape is lost, but the equilibrium is not reached as the ice continues to grow. The simulation would need to be run over multiple seasonal cycles, with winter-like sea ice growth followed by summer-like melt, to achieve an equilibrated ITDs. Nonetheless, we can still evaluate if these transient ITDs resemble winter-time observations, at least qualitatively.

The observed ITD is known to have an asymmetric shape that has been theoretically described using a gamma function distribution (Goff, 1995; Toppaladoddi & Wettlaufer, 2015) and the simulated ITD also resembles the gamma function distribution (Figure 14a, dashed line). While the shape of the ITD resembles observations, some of its quantitative metrics do not compare well. Specifically, Arctic-wide satellite-deduced FSD for a winter month, like February, has a mean of 1.7 m and a standard deviation of 0.77 m (Kwok et al., 2020). The simulated ITD reaches a similar mean of about 1.5 m, but the standard deviation is only about 0.4 m, significantly lower than observations. Of course, our model simulation is highly idealized, and the resulting ITD would depend on the imposed mechanical and thermodynamic forcing and model parameters, all of which could be tuned for a better match with observations. However, an important reason for the mismatch is that the observed ITD is composed of sea ice that is a mixture of first-year ice and multiyear ice, with a ratio of about 1.4:1 in February, while our model simulation only has first-year ice as it is run for a short amount of time. Since multiyear ice is typically thicker than first-year ice, its presence skews the ITD towards higher thicknesses and contributes to its large standard deviation. Considering these factors, the simulated ITD can be considered to be in qualitative agreement with observations. With a more elaborate experimental design, it might be possible to reach a quantitative agreement. Since this paper aims to introduce general SubZero capabilities, we envision many crucial process studies performed by the broader sea ice modeling community.

8 Summary and Discussion

We constructed a sea ice model that treats ice floes as discrete polygonal elements. Its main advantage, and the key difference from existing sea ice DEMs, is that SubZero's elements can change their shapes due to parameterized processes such as welding, fracturing, ridging, etc. Existing sea ice DEMs use fixed-shape elements (e.g., disks, rectangles, or tetrahedra), which can limit the interpretation of the model state when defining individual floes for comparison with data. Our model aims to bridge this gap and provide a framework that can be directly used to predict sea ice floe motion, either collectively in the form of floe size or thickness distributions or individually for each floe.

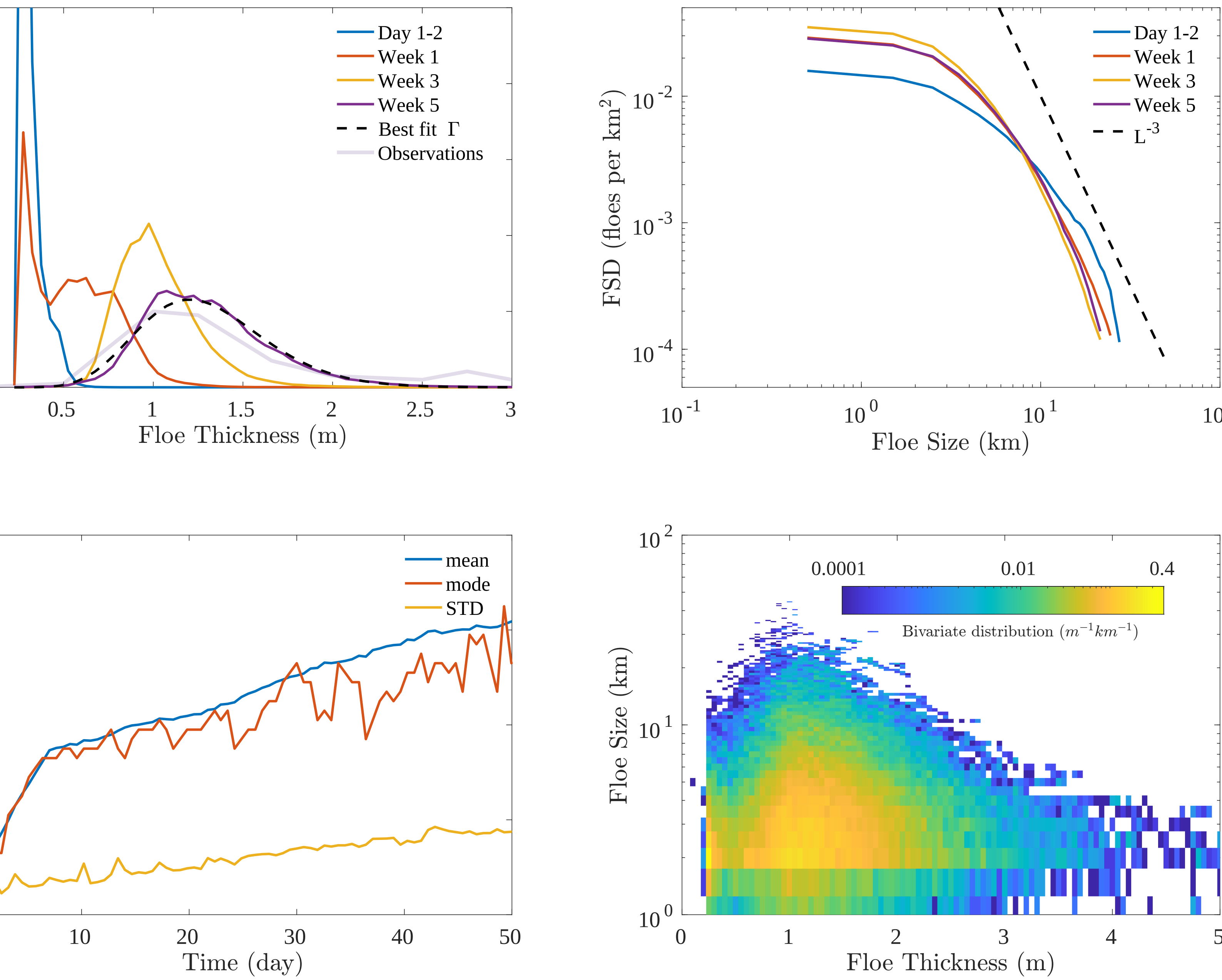

Figure 14. The evolution of floe size and thickness distributions for the winter simulation. **(a)** Ice thickness distribution (ITD) achieved in the early time after the initialization (blue), intermediate time (red), late time (orange) and at the end of the model simulation (purple); the best-fit gamma function is plotted for reference (dashed black line) and the lighter line shows observed thickness distribution via satellite. **(b)** Floe size distribution (FSD), plotted as the number of floes in a particular size bin per square kilometer; the L^{-3} power-law, L being the floe size, is shown for reference (dashed line). Note, floes smaller than 2 km^2 are not resolved in the simulation and only appear in the model as short-lived floes of recently fractured of larger floes. **(c)** Time evolution of the ITD mean, mode, and standard deviation. **(d)** Bivariate probability distribution of floes sizes and thicknesses, plotted for week 4 of the simulation.

We tested SubZero in several idealized scenarios to demonstrate its capabilities as a model of a granular and brittle material (the summer-time Nares Strait simulation) and a model with an active creation of new elements in addition to welding and fracture mechanics (the winter-time simulation). In both scenarios with idealized forcing and boundary conditions, the model-generated FSD had a power-law exponent ranging from about -2 (for pure fractures) to -3 for winter-like simulation. Both power-law exponents are well within the observed range. Similarly, during the winter-time sea ice growth simulations, the ice thickness distribution approached a qualitatively similar shape to the observed distribution, consisting of a single peak and an asymmetric tail for thicker sea ice. Since the model formulation specifies only the rules of floe interactions, one cannot guarantee that sensible equilibrated floe size and thickness distributions would emerge or that those would even remotely resemble the observed distributions. Yet, including only core processes with minimal parameter adjustment and using highly-idealized forcing and boundary conditions, the model approached a regime that resembles the observed sea ice behavior. This qualitative, and for many metrics, quantitative consistency with observations provides a substantial rationale for exploring various improvements to model physics. In particular, given its ability to explicitly simulate the floe life cycle, the philosophy behind SubZero strives to create a new generation of sea ice models.

We presented a proof of concept of a DEM with a varying number of elements that change their shapes subject to parameterized floe-scale physics. While the SubZero model already exhibits behavior consistent with sea ice observations, several improvements need to be made for it to become an operational sea ice model. Specifically, a more realistic formation of linear kinematic features could be achieved by developing more advanced floe fracture parameterizations, which would be an essential step toward mimicking floe-scale sea ice deformation. Another drawback of our model, and DEMs in general, is that its improved realism of floe dynamics is computationally demanding, and running such a model on basin scales presents a significant challenge. This issue could be addressed by improving the computational speed of the code using high-performance languages and GPU-enabled architectures. However, there will always be a limit to computing capabilities. Hence, to facilitate more accessible research and faster progress, developing computationally cheap basin-scale models would be necessary. One could envision theoretical studies attempting to formulate rescaled floe interaction rules (e.g., slightly modified contact laws, fracture rules) such that floes in the model would effectively represent clusters of floes of a particular scale. The problem of rescaling the floe interaction rules is tightly linked to the issue of representing the impact of unresolved floes and quantitatively defining what a floe represents in physical space. Even in its prototype-like state, SubZero is an attractive new sea ice model that could be valuable for idealized process studies and regional simulations.

We now comment on key distinctions of SubZero from existing continuous and discrete element sea ice models. Continuous rheology models, like viscous-plastic models (Hibler, 1979), are meant to represent basin-scale sea ice motion and formulated for length scales larger than 10–100 km to describe characteristics averaged over a large number of floes. Unlike the SubZero sea ice model, continuous rheology models do not provide direct information about the positions, sizes, and shapes of individual floes, but they could provide statistical information such as FSD and ITD by solving their evolution equations subject to parameterized physics. SubZero's output also can be presented in the form of Eulerian sea ice variables, like velocity or concentration. However, it is not a given that this discrete element model has equivalent continuous rheology describing the evolution of its Eulerian diagnostics. Hence, significant questions remain about using DEMs like SubZero to improve continuous sea ice models.

Comparing SubZero to existing sea ice DEMs, we can point out some key differences. A general concept behind DEMs is to use pre-defined element shapes (such as points, disks, rectangles, or tetrahedra) to simplify calculations of collisions. More complex structures can be formed as clusters of simple elements that are bonded together. But this comes at the expense of computing forces for those bonds, which is typically a stiff problem requiring small integration time steps. Consequently, it is challenging to use existing sea ice DEMs for long-term simulations to study equilibrium sea ice distributions (such as FSDs and ITDs). Instead, such models are commonly used to address problems where the sea ice state does not dramatically evolve from initial conditions, i.e., initial-value problems. SubZero bypasses the issue of using a large number of stiffly-connected simple elements by using complex floes with concave time-dependent shapes. Using complex floe shapes allows a straightforward creation of new elements in complex open-ocean regions between existing floes and simulating conditions with 100% ice cover using a modest number of floes. However, reducing the number of elements by transitioning to complex concave element shapes results in increased computational expense for resolving collisions and the need to parameterize floe-scale processes such as fractures and ridging. Parameterizations for the floe-scale processes could be derived by using the SubZero model by setting it up to resolve the sub-floe dynamics within individual floes; this approach is similar to nested runs used for resolving small-scale oceanic or atmospheric processes. The rationale behind SubZero's formulation is that it might be sufficient to use parameterized floe fractures and ridging (instead of explicitly resolving them) because these processes occur with high frequency and at a wide range of scales due to the highly varying and strong wind forcing typical for the Arctic Ocean. When only the statistical behavior of sea ice floes is of interest and exact details of individual fractures and ridging are not, a model like SubZero can effectively perform regional simulations of sea ice behavior at seasonal scales. Thus, SubZero demonstrates a new approach to floe-resolving sea ice modeling, being distinct from existing continuous and discrete element sea ice models. How the unique capabilities of the SubZero model could lead to our improved understanding of sea ice dynamics remains to be demonstrated in future studies.

9 Data Availability Statement

The most up to date SubZero code (Manucharyan & Montemuro, 2022) is provided at the public GitHub repository `https://github.com/SeaIce-Math/SubZero`. SubZero v1.0.1 (Montemuro & Manucharyan, 2022) associated with this publication and test cases shown above can be found on Zenodo `https://doi.org/10.5281/zenodo.7222680`.

Acknowledgments

G.E.M and B.P.M gratefully acknowledge support from the Office of Naval Research (ONR) grant N00014-19-1-2421. The authors highly appreciate the insightful discussions at the online workshop "Modeling the Granular Nature of Sea Ice" organized by the School of Oceanography, University of Washington as part of the ONR MURI project N00014-19-1-2421. The authors acknowledge high-performance computing support from Cheyenne (doi:10.5065/D6RX99HX) provided by NCAR's Computational and Information Systems Laboratory, sponsored by the National Science Foundation. The manuscript benefited greatly from the reviews provided by Anders Damsgaard, Martin Vancoppenolle, and an anonymous reviewer.

References

André, D., Jebahi, M., Iordanoff, I., luc Charles, J., & Néauport, J. (2013). Using the discrete element method to simulate brittle fracture in the indentation of a silica glass with a blunt indenter. *Computer Methods in Applied Mechanics and Engineering*, *265*, 136-147. doi: https://doi.org/10.1016/j.cma.2013.06.008

Boots, B., Sugihara, K., Chiu, S. N., & Okabe, A. (2009). Spatial tessellations: concepts and applications of voronoi diagrams.

Caflisch, R. E. (1998). Monte carlo and quasi-monte carlo methods. *Acta numerica*,

7, 1–49.
Chang, C. (1988). *Deformation behavior of sands under cyclic loading - a micro-structural approach* (Tech. Rep.). United States Air Force Office of Scientific Research.
Chen, N., Fu, S., & Manucharyan, G. (2021). Lagrangian data assimilation and parameter estimation of an idealized sea ice discrete element model. *Journal of Advances in Modeling Earth Systems*, *13*(10), e2021MS002513.
Coon, M. (1980). A review of aidjex modeling. *Sea ice processes and models*, *12*, 25.
Coon, M., Kwok, R., Levy, G., Pruis, M., Schreyer, H., & Sulsky, D. (2007). Arctic ice dynamics joint experiment (aidjex) assumptions revisited and found inadequate. *Journal of Geophysical Research: Oceans*, *112*(C11).
Cox, G., & Weeks, W. (1988). Numerical simulations of the profile properties of undeformed first-year sea ice during the growth season. *Journal of Geophysical Research: Oceans*, *93*(C10), 12449–12460.
Cundall, P. A., & Strack, O. D. (1979). A discrete numerical model for granular assemblies. *geotechnique*, *29*(1), 47–65.
Damsgaard, A., Adcroft, A., & Sergienko, O. (2018). Application of discrete element methods to approximate sea ice dynamics. *Journal of Advances in Modeling Earth Systems*, *10*(9), 2228–2244.
Damsgaard, A., Sergienko, O., & Adcroft, A. (2021). The effects of ice floe-floe interactions on pressure ridging in sea ice. *Journal of Advances in Modeling Earth Systems*, *13*(7), e2020MS002336.
Denton, A. A., & Timmermans, M.-L. (2021). Characterizing the sea-ice floe size distribution in the canada basin from high-resolution optical satellite imagery. *The Cryosphere Discussions*, *2021*, 1–20. doi: 10.5194/tc-2021-368
Feltham, D. L. (2008). Sea ice rheology. *Annu. Rev. Fluid Mech.*, *40*, 91–112.
Feng, Y., Han, K., & Owen, D. (2012). Energy-conserving contact interaction models for arbitrarily shaped discrete elements. *Computer methods in applied mechanics and engineering*, *205*, 169–177.
Goff, J. A. (1995). Quantitative analysis of sea ice draft: 1. methods for stochastic modeling. *Journal of Geophysical Research: Oceans*, *100*(C4), 6993–7004.
Grima, A. P., & Wypych, P. W. (2011). Development and validation of calibration methods for discrete element modelling. *Granular Matter*, *13*(2), 127–132.
Gutfraind, R., & Savage, S. B. (1997). Smoothed particle hydrodynamics for the simulation of broken-ice fields: Mohr–coulomb-type rheology and frictional boundary conditions. *Journal of Computational Physics*, *134*(2), 203–215.
Herman, A. (2013). Numerical modeling of force and contact networks in fragmented sea ice. *Annals of Glaciology*, *54*(62), 114–120. doi: 10.3189/2013AoG62A055
Herman, A. (2016). Discrete-element bonded-particle sea ice model design, version 1.3 a–model description and implementation. *Geoscientific Model Development*, *9*(3), 1219–1241.
Herman, A., Cheng, S., & Shen, H. H. (2019). Wave energy attenuation in fields of colliding ice floes–part 1: Discrete-element modelling of dissipation due to ice–water drag. *The Cryosphere*, *13*(11), 2887–2900.
Hibler, W. D. (1979). A dynamic thermodynamic sea ice model. *Journal of physical oceanography*, *9*(4), 815–846.
Hibler III, W. (1977). A viscous sea ice law as a stochastic average of plasticity. *Journal of Geophysical Research*, *82*(27), 3932–3938.
Hibler III, W. (1980). Modeling a variable thickness sea ice cover. *Monthly weather review*, *108*(12), 1943–1973.
Hibler III, W., & Schulson, E. M. (2000). On modeling the anisotropic failure and flow of flawed sea ice. *Journal of Geophysical Research: Oceans*, *105*(C7), 17105–17120.
Holt, B., & Martin, S. (2001). The effect of a storm on the 1992 summer sea ice

cover of the beaufort, chukchi, and east siberian seas. *Journal of Geophysical Research: Oceans*, *106*(C1), 1017–1032.

Hopkins, M. A. (1996). On the mesoscale interaction of lead ice and floes. *Journal of Geophysical Research: Oceans*, *101*(C8), 18315-18326. doi: https://doi.org/10.1029/96JC01689

Hopkins, M. A. (1998). Four stages of pressure ridging. *Journal of Geophysical Research: Oceans*, *103*(C10), 21883–21891.

Hopkins, M. A., Frankenstein, S., & Thorndike, A. S. (2004). Formation of an aggregate scale in arctic sea ice. *Journal of Geophysical Research: Oceans*, *109*(C1).

Hopkins, M. A., Tuhkuri, J., & Lensu, M. (1999). Rafting and ridging of thin ice sheets. *Journal of Geophysical Research: Oceans*, *104*(C6), 13605–13613.

Horvat, C., Roach, L. A., Tilling, R., Bitz, C. M., Fox-Kemper, B., Guider, C., ... Shepherd, A. (2019). Estimating the sea ice floe size distribution using satellite altimetry: theory, climatology, and model comparison. *The Cryosphere*, *13*(11), 2869–2885.

Hutchings, J. K., Roberts, A., Geiger, C. A., & Richter-Menge, J. (2011). Spatial and temporal characterization of sea-ice deformation. *Annals of Glaciology*, *52*(57), 360–368.

Hutter, N., Bouchat, A., Dupont, F., Dukhovskoy, D., Koldunov, N., Lee, Y. J., ... others (2022). Sea ice rheology experiment (sirex): 2. evaluating linear kinematic features in high-resolution sea ice simulations. *Journal of Geophysical Research: Oceans*, *127*(4), e2021JC017666.

Hutter, N., & Losch, M. (2020). Feature-based comparison of sea ice deformation in lead-permitting sea ice simulations. *The Cryosphere*, *14*(1), 93–113.

Kawamoto, R., Andò, E., Viggiani, G., & Andrade, J. E. (2016). Level set discrete element method for three-dimensional computations with triaxial case study. *Journal of the Mechanics and Physics of Solids*, *91*, 1–13.

Keen, A., Blockley, E., Bailey, D. A., Boldingh Debernard, J., Bushuk, M., Delhaye, S., ... others (2021). An inter-comparison of the mass budget of the arctic sea ice in cmip6 models. *The Cryosphere*, *15*(2), 951–982.

Kulchitsky, A., Hutchings, J., Johnson, J., & Lewis, B. (2017). *Siku sea ice discrete element method model* (Tech. Rep.). University of Alaska Fairbanks and Oregon State University.

Kwok, R., Kacimi, S., Webster, M., Kurtz, N., & Petty, A. (2020). Arctic snow depth and sea ice thickness from icesat-2 and cryosat-2 freeboards: A first examination. *Journal of Geophysical Research: Oceans*, *125*(3), e2019JC016008. doi: https://doi.org/10.1029/2019JC016008

Kwok, R., Toudal Pedersen, L., Gudmandsen, P., & Pang, S. S. (2010). Large sea ice outflow into the nares strait in 2007. *Geophysical Research Letters*, *37*(3). doi: https://doi.org/10.1029/2009GL041872

Lemke, P., Trinkl, E., & Hasselmann, K. (1980). Stochastic dynamic analysis of polar sea ice variability. *Journal of Physical Oceanography*, *10*(12), 2100–2120.

Leppäranta, M. (1993). A review of analytical models of sea-ice growth. *Atmosphere-Ocean*, *31*(1), 123–138.

Lindsay, R., & Stern, H. (2004). A new lagrangian model of arctic sea ice. *Journal of physical oceanography*, *34*(1), 272–283.

Liu, L., & Ji, S. (2018). Ice load on floating structure simulated with dilated polyhedral discrete element method in broken ice field. *Applied Ocean Research*, *75*, 53–65.

Luding, S. (2008). Introduction to discrete element methods: basic of contact force models and how to perform the micro-macro transition to continuum theory. *European journal of environmental and civil engineering*, *12*(7-8), 785–826.

Manucharyan, G., & Montemuro, B. (2022). *Subzero sea ice model.* `https://github.com/SeaIce-Math/SubZero`. GitHub.

Marin, J. (1984). Computing columns, footings and gates through moments of area. *Computers & Structures*, *18*(2), 343–349.

Marquis, O., Tremblay, B., Lemieux, J.-F., & Islam, M. (2022). Smoothed particle hydrodynamics implementation of the standard viscous-plastic sea-ice model and validation in simple idealized experiments. *The Cryosphere Discussions*, 1–33.

Mehlmann, C., Danilov, S., Losch, M., Lemieux, J.-F., Hutter, N., Richter, T., ... Korn, P. (2021). Simulating linear kinematic features in viscous-plastic sea ice models on quadrilateral and triangular grids with different variable staggering. *Journal of Advances in Modeling Earth Systems*, *13*(11), e2021MS002523.

Mohammadi-Aragh, M., Losch, M., & Goessling, H. F. (2020). Comparing arctic sea ice model simulations to satellite observations by multiscale directional analysis of linear kinematic features. *Monthly Weather Review*, *148*(8), 3287–3303.

Monaghan, J. J. (1992). Smoothed particle hydrodynamics. *Annual review of astronomy and astrophysics*, *30*(1), 543–574.

Montemuro, B., & Manucharyan, G. (2022, October). *Subzero v1.0.1.* Zenodo. Retrieved from `https://doi.org/10.5281/zenodo.7222680` doi: 10.5281/zenodo.7222680

Montiel, F., & Squire, V. A. (2017). Modelling wave-induced sea ice break-up in the marginal ice zone. *Proceedings of the Royal Society A: Mathematical, Physical and Engineering Sciences*, *473*(2206), 20170258.

Moore, G., Howell, S., Brady, M., Xu, X., & McNeil, K. (2021). Anomalous collapses of nares strait ice arches leads to enhanced export of arctic sea ice. *Nature communications*, *12*(1), 1–8.

Oberle, W. (2015). *Monte carlo simulations: number of iterations and accuracy* (Tech. Rep.). Army Research Lab Aberdeen Proving Ground MD Weapons and Materials Research ....

Parmerter, R. R. (1975). A model of simple rafting in sea ice. *Journal of Geophysical Research (1896-1977)*, *80*(15), 1948-1952. doi: https://doi.org/10.1029/JC080i015p01948

Percival, D., Rothrock, D., Thorndike, A., & Gneiting, T. (2008). The variance of mean sea-ice thickness: Effect of long-range dependence. *Journal of Geophysical Research: Oceans*, *113*(C1).

Perovich, D. K., & Jones, K. F. (2014). The seasonal evolution of sea ice floe size distribution. *Journal of Geophysical Research: Oceans*, *119*(12), 8767–8777.

Potyondy, D. O., & Cundall, P. (2004). A bonded-particle model for rock. *International journal of rock mechanics and mining sciences*, *41*(8), 1329–1364.

Radjai, F., & Dubois, F. (2011). *Discrete-element modeling of granular materials.* Wiley-Iste.

Rampal, P., Weiss, J., Marsan, D., & Bourgoin, M. (2009). Arctic sea ice velocity field: General circulation and turbulent-like fluctuations. *Journal of Geophysical Research: Oceans*, *114*(C10).

Roach, L. A., Horvat, C., Dean, S. M., & Bitz, C. M. (2018). An emergent sea ice floe size distribution in a global coupled ocean-sea ice model. *Journal of Geophysical Research: Oceans*, *123*(6), 4322–4337.

Rothenburg, L., & Selvadurai, A. (1981). A micromechanical definition of the cauchy stress tensor for particulate media. *Mechanics of structured media : proceedings of the International symposium on the Mechanical Behaviour of Structured Media*, *b*, 469-486.

Rothrock, D., & Thorndike, A. (1984). Measuring the sea ice floe size distribution. *Journal of Geophysical Research: Oceans*, *89*(C4), 6477–6486.

Semtner Jr, A. J. (1976). A model for the thermodynamic growth of sea ice in numerical investigations of climate. *Journal of Physical Oceanography*, *6*(3), 379–389.

Shen, H. H., & Ackley, S. F. (1991). A one-dimensional model for wave-induced ice-floe collisions. *Annals of Glaciology*, *15*, 87–95.

Stern, H. L., Schweiger, A. J., Zhang, J., & Steele, M. (2018, 07). On reconciling disparate studies of the sea-ice floe size distribution. *Elementa: Science of the Anthropocene*, *6*. doi: 10.1525/elementa.304

Toppaladoddi, S., & Wettlaufer, J. S. (2015, Oct). Theory of the sea ice thickness distribution. *Phys. Rev. Lett.*, *115*, 148501. doi: 10.1103/PhysRevLett.115.148501

Toyota, T., Takatsuji, S., & Nakayama, M. (2006). Characteristics of sea ice floe size distribution in the seasonal ice zone. *Geophysical research letters*, *33*(2).

Tuhkuri, J., & Lensu, M. (2002). Laboratory tests on ridging and rafting of ice sheets. *Journal of Geophysical Research: Oceans*, *107*(C9), 8–1.

Tuhkuri, J., & Polojärvi, A. (2018). A review of discrete element simulation of ice–structure interaction. *Philosophical Transactions of the Royal Society A: Mathematical, Physical and Engineering Sciences*, *376*(2129), 20170335.

Turner, A. K., Peterson, K. J., & Bolintineanu, D. (2022). Geometric remapping of particle distributions in the discrete element model for sea ice (demsi v0. 0). *Geoscientific Model Development*, *15*(5), 1953–1970.

Weiss, J., & Schulson, E. M. (2009, oct). Coulombic faulting from the grain scale to the geophysical scale: lessons from ice. *Journal of Physics D: Applied Physics*, *42*(21), 214017. doi: 10.1088/0022-3727/42/21/214017

West, B., O'Connor, D., Parno, M., Krackow, M., & Polashenski, C. (2021). Bonded discrete element simulations of sea ice with non-local failure: Applications to nares strait. *Journal of Advances in Modeling Earth Systems*, e2021MS002614.

Wilchinsky, A. V., Feltham, D. L., & Hopkins, M. A. (2010). Effect of shear rupture on aggregate scale formation in sea ice. *Journal of Geophysical Research: Oceans*, *115*(C10).

Zhang, J., Schweiger, A., Steele, M., & Stern, H. (2015). Sea ice floe size distribution in the marginal ice zone: Theory and numerical experiments. *Journal of Geophysical Research: Oceans*, *120*(5), 3484–3498.